# Supplementary Information

**Hominin presence in Eurasia by at least 1.95 Ma**

Sabrina C. Curran[1]*†, Virgil Drăguşin[2], Briana Pobiner[3], Michael Pante[4], John Hellstrom[5], Jon Woodhead[5], Roman Croitor[6], Adrian Doboș[7], Samantha E. Gogol[8], Vasile Ersek[9], Trevor L. Keevil[3], Alexandru Petculescu[2], Aurelian Popescu[10], Chris Robinson[11,12], Lars Werdelin[13], Claire E. Terhune[14]†

Corresponding authors: currans@ohio.edu and cterhune@uark.edu

**Table of Contents**

**Supplementary Notes**

Supplementary Note 1: Biochronological Framework of the ORV

The geological and biostratigraphical context for the Olteţ River Valley (ORV) sites has been best described previously by Radulesco and Samson[1] and Andreescu et al.[2,3]. The fossil localities examined or discussed as part of this study—Grăunceanu, La Pietriș, Valea Roșcăi, Dealul Mijlociu, and Fântâna lui Mitilan—all stem from the Tetoiu Formation, originally defined by Andreescu et al.[2]. This formation is described as a richly fossiliferous set of deposits in a sandy-pebbly facies, predominately situated in the Olt-Olteţ interfluve. Thickness of the formation varies across its extent but generally increases as it progresses south; maximum thickness at its southern-most margin is ~150 m. Before the Tetoiu Formation was officially described, these sediments were discussed by Radulesco and Samson[1] in the context of the fossil sites of the ORV. They outline three faunal horizons situated in a series of fluvio-lacustrine sequences. Their lower faunal horizon (T-1) includes multiple sites evaluated here (Valea Roșcăi, La Pietriș, Dealul Mijlociu, and Grăunceanu), all of which are situated lower in the stratigraphic portion of the described sequence. These authors assigned this faunal horizon (on the basis of biochronology) to MN17; work by Andreescu et al.[2,3] suggests this horizon is approximately 1.95 Ma. Radulesco and Samson's second faunal horizon (T-2), which is situated ~50 m above sites from T-1, includes Fântâna lui Mitilan and Fântâna Alortetei (the latter of which is not included here, but which is mentioned in other papers by our research team). Sites from T-2 have a distinctly different, and younger, fauna than those in T-1; Radulesco and Samson[1] assign these to MNQ18 and Andreescu et al.[2,3] suggest this horizon is ~1.5 Ma. The youngest horizon (T-3) is ~30 m above T-2 and includes multiple sites not discussed here. Radulesco and Samson[1] assigned this horizon to MNQ 19/20 on the basis of biochronological assessments of the fauna, which corresponds to ~1.3 Ma according to Andreescu et al.[2,3].

Supplementary Note 2: ORV Lithics

Two lithics have been reported from the locality of Dealul Mijlociu[4,5]. This site is in relatively close proximity to Grăunceanu (1.5 km), lying along the same valley/ridge complex (approximately midway between Grăunceanu and La Pietriș). Deposits at the site were originally described by Radulesco and Samson[1] as a layer of sand and gravel belonging to the same lower faunal horizon as both La Pietriş and Grăunceanu.

Our team relocated the lithics and one of us (AD) reanalyzed these tools. They are described as:

- DMJ.0001 (Supplementary Fig. 1): This specimen is a single-surface core manufactured from brown flint. Dimensions are 5.6 x 3.9 x 3 cm. Between 10-40% of the surface retains the cortex, which is alluvial in nature. One side preserves the negative of a preferential flake.
- DMJ.0002 (Supplementary Fig. 1): This specimen is a chopping-tool manufactured from brown flint. Dimensions are 5.5 x 4.3 x 2.6 cm. Between 10-40% of the surface retains the cortex, which is alluvial in nature. One side of the piece has a retouched notch.

Prior publications described the core (DMJ.0001) as a proto-biface[4,5] and subsequently reproduced as such by [6]. For both pieces, the flake scars have fairly rounded ridges, with some edge damage that is consistent with being exposed to post-depositional processes. Unfortunately,

neither piece provides clear chrono-cultural markers making it difficult to definitively assign an age to these lithics based solely on their morphology.

Supplementary Note 3: Taphonomic Analysis

A full assessment of all taphonomic signatures present in the ORV assemblage is in preparation and briefly summarized here. Specimens from Grăunceanu are not heavily affected by weathering (85% of specimens are in weathering stage 0[7]). The majority of specimens (73%) have 75-100% surface visibility. In general, the Grăunceanu assemblage is most heavily altered by post-depositional processes, particularly root-etching and abiotic damage associated with burial and fossilization. Some evidence of root etching is present on 82% of specimens from Grăunceanu, 42% exhibit some type of post-depositional damage (chipping, pitting, cracking, surface exfoliation), and 27% have some adhering matrix and/or manganese staining. There is little evidence of water-based alterations, with only 0.46% of specimens presenting any smoothed or rounded features. 9.5% of the assemblage exhibited some form of carnivore damage (tooth scores, pits, crenulations, etc.). The assemblage also shows some evidence (<2%) of insect damage and rodent gnawing. A total of 1,189 (26.3%) specimens with linear marks were identified from Grăunceanu. Of these, 296 specimens have marks identified as excavator or preparator damage, 290 specimens have marks identified as carnivore tooth scores, 172 specimens have marks identified as sedimentary abrasion or trampling, and 20 have marks identified as cut marks; the remaining (411) marks were not able to be categorized.

Supplementary Note 4: Quantitative Analyses of Cut Marks

A total of 32 individual marks were measured from 17 separate specimens using the above-described methods. A quadratic discriminant analysis (QDA), using experimental data with high classificatory success (see Supplemental Fig. 23 for PCA, Supplementary Fig. 24 for ROC curve, and Supplementary Table 1 for 10-fold and leave-one-out cross-validation QDA confusion matrix), classified 22 marks as cut marks, 4 as tooth marks, and 6 as trample marks (Supplementary Data 2, Supplementary Fig. 22). Marks identified as cut marks had posterior probabilities that ranged between 0.57 and 1.0, with values closer to one indicating a higher level of certainty in the model's classification. Some marks that were qualitatively identified as cut marks had primary IDs of trample or tooth, but these cases were frequently secondarily identified as cut marks (i.e., secondary posterior probabilities ranging from 0.12 to 0.39).

A leave-one-out cross-validation test shows that experimental cut marks were most likely to be confused with sedimentary abrasion/trampling marks (5.7% incorrectly classified) and tooth marks (4.9% incorrectly classified), though cut marks were correctly classified 89.4% of the time[8] (Supplementary Table 1).

Supplementary Note 5: Detailed Description of Cut Marks

All cut marks discussed here (Fig. 2, Supplementary Figs. 2-21, Supplementary Data 2) have the same color inside the mark as on the rest of the bone's surface, lack barbs, and lack shoulder effects (except for VGr.0519). Only two have curved trajectories (VGr.0091 and VGr.1490), though several have a slight curve. Other attributes vary as discussed for each specimen.

*High-Confidence Cut Marks*

- VGr.0076 (Supplementary Fig. 2; Marks A and C) is a partial (proximal metaphysis through distal diaphysis) right tibia of a small carnivore. Its surface has high visibility, with limited root etching and is at weathering stage 0. The marks we identify as being high-confidence cut marks are two of four marks discussed here, with the other two discussed below as probable cut marks. These marks have a straight trajectory and are oriented obliquely to the long axis of the bone on the posterior of the mid-diaphysis, consistent with filleting the gastrocnemius[9]. Both marks were identified as cut marks in the quantitative analysis with high posterior probabilities (0.966 and 0.964).
- VGr.0519 (Supplementary Fig. 3) is a partial (mid-diaphysis to distal epiphysis) right tibia of an artiodactyl. Its surface has high visibility, with some root etching and is at weathering stage 0. Two deep and parallel marks are located on the posterior distal metaphysis that have transverse orientations to the long axis of the bone, straight trajectories, u-shape and asymmetrical cross-sections, with shoulder-effects present. Mark A was included in the quantitative analysis and identified as a cut mark with a posterior probability of 0.788. Mark B suffered from more bioerosion (root etching) than Mark A and was identified in the quantitative analysis as a tooth score. However, it shares the same qualitative features as Mark A and is thus considered to be of the same origin. Marks on distal tibiae have been found to be produced in both skinning and filleting[9].
- VGr.1483 (Supplementary Fig. 4) is a partial (distal metaphysis to distal epiphysis) left tibia of a cervid. Its surface has high visibility, with possible insect damage and is at weathering stage 0. On the medial malleolus is a cluster of ~10 parallel marks that run slightly obliquely to the orientation of the bone's long axis. The marks all have straight trajectories and symmetrical v-shaped cross-sections. Qualitative analyses firmly support these marks as cut marks, while the quantitative analysis is less certain, identifying it as cut mark with a relatively low posterior probability of 0.571. It is worth noting that the quantitative sample primarily includes marks located on limb bone midshafts, whereas this mark is located on a limb bone epiphysis, which likely impacted mark morphology and depth. The depth of the mark is closer to that of tooth marks in the comparative sample, while its v-shaped cross-section, indicated by an acute opening angle, is more typical of cut marks.
- VGr.1515 (Supplementary Fig. 5) is a partial (distal metaphysis to distal epiphysis) right tibia of an artiodactyl. Its surface has high visibility, with possible insect damage and is at weathering stage 0. Two parallel marks located on the medial malleolus run oblique to the long axis of the bone, have straight trajectories and wide v-shaped (_/), and symmetrical cross-sections. Both qualitative and quantitative methods identify these marks as cut marks (with posterior probabilities of 0.919 for Mark A and 0.813 for Mark B).
- VGr.2004 (Supplementary Fig. 6) is a vertebrate bone fragment with ~9 visible linear marks. The surface has high visibility and is in weathering stage 0, but does display traces of root etching, carnivore chewing and pits. The marks run along the length of the fragment in transverse orientation to the long axis of the bone, with straight trajectories, v-shaped and symmetrical cross-sections, and have micro-striations present. Quantitative analyses identified three of these marks as cut marks with high posteriors (Mark A= 0.971 and Mark B= 1.0, Mark C = 0.834) while one other was identified as a trample

mark with a posterior probability of 0.879 (and as cut mark as a secondary identification). As with VGr.0519, since these marks are parallel and present nearly identical qualitative attributes, we include them all in our high-confidence cut mark category.

- VGr.2170 (Supplementary Fig. 7) is a partial (proximal metaphysis to distal metaphysis) right humerus of an artiodactyl. Its surface has high visibility, with some root etching and is at weathering stage 0. There are four visible linear marks on the medial distal metaphysis that are obliquely oriented to the long axis of the bone, which is consistent with filetting[9]. The marks have straight trajectories and _/ and v-shaped and symmetrical cross-sections. Both qualitative and quantitative methods identify these marks as cut marks. Quantitative analysis identified Mark A as a cut mark with a posterior probability of 0.973 and Mark B as a cut mark with a posterior probability of 0.800.
- VGr.2649 (Supplementary Fig. 8) is a vertebrate long bone fragment. Its surface has high visibility, with some root etching and is at weathering stage 0. Five parallel linear marks are visible in a cluster that have nearly transverse orientation to the long axis of the bone. Two marks were included in the quantitative analysis. Mark A was identified as a tooth score, though with a relatively low posterior probability (0.650), which is supported by our qualitative analysis in which we assigned this mark to our "unknown mark" category. Mark B presents more consistent cut mark features, with a straight trajectory and a symmetrical cross-section, and was identified in the quantitative analysis as a cut mark (posterior probability = 0.930).
- Only one non-Grăunceanu specimen was identified as having high-confidence cut marks. This specimen, FM.0091 (Supplementary Fig. 9), is from Fântâna lui Mitilan and is the right side of a mandible from *Eucladoceros* sp. with high visibility to its surface, though it is in weathering stage 1 and has some root etching and exfoliation of its surface. Two very long and parallel linear marks run almost the length of the mandibular corpus with a somewhat curved trajectory. Their cross-sections vary from u- to v-shaped and are asymmetrical. Quantitative analysis identified Mark A and Mark B as cut marks with posterior probabilities of 0.988 and 0.726, respectively. The location of these marks does not correspond to patterns of butchery described by [9], though it is possible that they were made when the buccal mucosa was separated from the mandible.

*Probable Cut Marks*

- VGr.0076 (Supplementary Fig. 2) is the same specimen as reported above as having two high-confidence cut marks. This specimen has several other linear marks that present some qualitative features consistent with cut mark morphology, however two (Marks B and D) were identified as trampling in the quantitative analysis. Thus, we have assigned these specific marks to the lower-confidence (probable) category.
- VGr.0351c (Supplementary Fig. 10) is a partial (proximal through mid-diaphysis) right femur of a subadult *Paradolichopithecus arvernensis*. Its surface has high visibility, with some root etching, sedimentary abrasion, adhering matrix, possible tooth scores, and shellac applied (though not to the mark itself) and is at weathering stage 0. Two parallel linear marks with straight trajectories are visible on the posterior of the mid-diaphysis and have a slightly oblique orientation to the long axis of the bone. Due to an error in the molding process, this specimen was not included in the quantitative analysis, thus we identify it to only the lower confidence level of probable cut mark. The location of these marks is consistent with filleting.

- VGr.0397 (Supplementary Fig. 11) is a complete right *Equus* sp. metacarpal. It has high surface visibility, though it is in weathering stage 1 and has slight root etching and sedimentary abrasion. Two parallel linear marks on the anterolateral distal metaphysis run slightly oblique to the long axis of the bone and are crossed by root etching, cracking, and some smoothing. These marks have slightly curved trajectories with v-shaped and symmetrical cross-sections. Both qualitative and quantitative (posterior probability of 0.997) methods identify these marks as cut marks, though at lower confidence due to the surface erosion of the specimen. Since there is no meat on the metacarpal, these marks are likely related to skinning.
- VGr.0429 (Supplementary Fig. 12) is a partial metapodial (single distal condyle) of a cervid. The surface has high visibility and is in weathering stage 0, with traces of root etching. A very deep linear mark (which has a shape similar to a percussion notch) is located on the superior portion of the condyle in a slightly oblique orientation. This mark (Mark A) has a straight trajectory and a v-shaped and symmetrical cross-section. The quantitative analysis identified the mark as a tooth score (posterior probability = 0.545) and gave a secondary identification of percussion mark (posterior probability = 0.21). A second mark was identified during the quantitative analysis, but it has very few features associated with cut marks, and as such we identify this mark as a mark of unknown origin. Given the location and depth of Mark A, it likely resulted from disarticulation.
- VGr.0591 (Supplementary Fig. 13) is a partial (proximal diaphysis to distal metaphysis) left humerus of an artiodactyl. It has high surface visibility, though it is in weathering stage 1 and has slight root etching and adhering matrix. A cluster of ~5 linear marks run in oblique orientation on the posterior mid-diaphysis and are consistent with filleting. These marks have slightly curved trajectories with u-shaped and asymmetrical cross-sections and have micro-striations present. The quantitative analysis identified one of these marks as a trample mark with low confidence (posterior probability = 0.501) with cut mark as its secondary identification (posterior probability = 0.393).
- VGr.1490 (Supplementary Fig. 14) is a partial (proximal to distal diaphysis) metapodial of an artiodactyl. Its surface has high visibility, with some root etching and is at weathering stage 0. A single linear mark is present running obliquely along the shaft that has a curved trajectory, a v-shaped and asymmetrical cross-section, and has microstriations present. Both qualitative and quantitative methods identify this mark as a cut mark (posterior probability = 0.997). The mark's location suggests it was created during tendon removal[10].
- VGr.1557 (Supplementary Fig. 15) is a partial (proximal epiphysis to distal diaphysis) left metatarsal of a cervid that has been broken into several pieces. Its surface has reduced visibility due to high root etching and slight weathering (stage 1), though the linear marks themselves are clear. Two parallel linear marks that run transversely are found on a broken piece of the specimen that have straight trajectories with adhering matrix within the marks. Mark A was identified as a trampling mark in the quantitative analysis and Mark B was not included in the quantitative analysis. Due to its incompleteness, the location of the mark cannot be identified completely, though it is possible that it was also created during tendon removal.
- VGr.1594 (Supplementary Fig. 16) is a partial (proximal epiphysis to distal diaphysis) right cervid metacarpal. Its surface has reduced visibility due to root etching and slight weathering (stage 1). Two linear marks are visible on the anterior side of the proximal

metaphysis that have transverse orientation to the long axis of the bone. Mark A was identified as a mark of unknown origin due to its slightly curved trajectory and because it was too eroded to include in the quantitative analysis. Mark B was identified as a cut mark with high posterior probability (0.970) in the quantitative analysis. Given the marks' location on the anterior aspect of the metacarpal, they were likely made during skinning.

- VGr.1767 (Supplementary Fig. 17) is a nearly complete (proximal through distal metaphysis) left tibia of a juvenile artiodactyl with very high root etching. However, the root etching does penetrate all aspects of the two linear marks on the distal diaphysis, and they could not be included in the quantitative analysis. These two marks are parallel to each other and obliquely oriented to the long axis of the shaft, consistent with either skinning or filleting[9]. They are straight with no visible barbs, though any shoulder effects or striations would have been obliterated by the root etching.
- VGr.2052 (Supplementary Fig. 18) is a fragmented mandible of *Stephanorhinus* sp. that has a fairly degraded bone surface. Though it is only at weathering stage 1, the surface has a slight chalky texture and has matrix adhering to it. A single linear mark runs oblique to the long axis of the mandibular corpus with a somewhat straight trajectory and a u-shaped and symmetrical cross-section. This mark was identified in the quantitative analysis as a cut mark with a high posterior probability (0.903) and we consider this mark to be a probable cut mark despite the degraded bone surface.
- VGr.2186 (Supplementary Fig. 19) is a partial (proximal epiphysis to mid-diaphysis) right radius of an artiodactyl. The surface has high visibility though it is in weathering stage 1, with traces of root etching. Along the anterior mid-diaphysis there is a patch of ~15 small and parallel linear marks obliquely oriented to the long axis of the bone that have straight trajectories. These marks are too shallow for observation of their internal morphology and could not be scanned for the same reason. They are consistent with filleting.
- VGr.2275 (Supplementary Fig. 20) is a partial (proximal metaphysis to mid-diaphysis) subadult artiodactyl tibia. Its surface is somewhat challenging to read due to its juvenile status and extensive root etching, however, there are four visible linear marks along the anterior side of the mid-diaphysis. This location could indicate either skinning or disarticulation. These marks have straight to slightly curved trajectories, are transversely oriented to the long axis of the bone and have v-shaped and symmetrical cross-sections. Of the three marks for which scans could be created, two were identified as cut marks (Mark B and Mark C, with posterior probabilities of 0.990 and 1.0, respectively), while the other mark was identified as trampling (Mark A, posterior probability = 0.930).
- VGr.2687 (Supplementary Fig. 21) is a vertebrate bone fragment with root etching and some surface degradation in weathering stage 0. Two linear marks are present on this specimen that have transverse orientation to the long axis of the fragment, straight trajectories, and cross-sections that are v-shaped and asymmetrical. Both qualitative and quantitative methods identify these marks as cut marks.

Supplementary Note 6: Interpretation of U-Pb Results

Biogenic apatites are highly susceptible to secondary element mobility upon burial; these open system effects are particularly visible in the REE and U. The latter forms a significant impediment to U-Th and U-Pb dating methodologies for which teeth would otherwise seem

ideally suited[11]. In the case of relatively simple U uptake histories it is possible to model U diffusion profiles to allow correction for these effects, and this methodology has been used with some success (e.g.,[12-14], although it is relatively time-consuming and thus not ideally suited to large sampling campaigns. Furthermore, for samples with a more complex diagenetic history, even modeling of this kind may not provide an adequate correction for U mobility effects. We note, however, in older samples—especially those beyond the range of the U-Th chronometer—that teeth from some locations do provide very well constrained U-Pb isochrons (e.g.,[15], as is the case for many of our samples. In these cases, teeth may well have experienced post-depositional U-uptake immediately upon burial often resulting in abnormally high U contents (the so-called 'early uptake' model), but it is clear from the quality of the isochrons (Supplementary Fig. 26) obtained here that a closed system condition with little subsequent U migration must have rapidly been attained. Studies are now emerging that offer the potential for identification of those samples most likely to produce meaningful U-Pb ages (e.g.,[16] but we note that these methods require pre-screening via laser ablation protocols. As a result, we find it equally productive to simply perform rapid reconnaissance U-Pb measurements using ~10 spots per sample for the identification of 'well behaved' samples before proceeding to full isochron construction which may require upwards of ~30 spots per sample; this was the protocol we employed here.

We observed a mixture of responses among the ORV teeth that we have studied. Some are extraordinarily low in U and may have experienced no post-depositional uptake (but are equally unsuited to dating due to low U/Pb ratios), others provide scattered distributions on U-Pb isochron plots indicating multiple episodes of, or continuous, element mobility, while others produce remarkably coherent U-Pb isochrons of high quality. Only the latter examples are reported here and, for these, we interpret these ages as those of early diagenesis with subsequent burial in a reducing or dry environment, limiting further U mobility.

Importantly, for future studies, we typically observe that tooth enamel (which is often considered the best-preserved material for some studies due to its low porosity e.g. Sr isotope tracing) appears to be very poorly suited to geochronology with low U and quite often high Pb contents. In contrast, the rapid post-mortem uptake of U in dentine tissue produces highly radiogenic analyses that consequently allow for precise age estimates. After some initial experimentation, all of the analyses reported here were performed on dentine tissue.

For relatively young (from the perspective of U–Pb geochronology) samples such as these, U-Pb ages should be corrected for the effects of initial disequilibrium in the series of intermediate daughter nuclides that runs from $^{238}U$ to $^{206}Pb$ [17]. This requires either knowledge of the $^{234}U/^{238}U$ ratio at time of sample burial or a measurement of $^{234}U/^{238}U$ of the sample today. The exponential nature of radioactive decay means that relatively small recent perturbations in the U content of a sample can have a large effect on ages and age corrections calculated using U-series disequilibrium equations, whilst not being significant enough to affect U-Pb isochron ages themselves.

The twenty $^{238}U$-$^{234}U$-$^{230}Th$ measurements on micro-drilled samples were plotted on a $^{234}U/^{238}U$ vs $^{230}Th/^{238}U$ isochron diagram (Supplementary Fig. 26). Six samples were within their 2σ uncertainty of the infinite age isochron; in other words, these samples were considered to show no evidence of recent uranium mobility. These gave a mean $^{234}U/^{238}U$ activity ratio of 1.0039 ±

0.0035 (2 s.d.) and gave excellent replication where two of these were from the same tooth. Eleven samples gave apparent U-Th ages of 430 ka or less which cannot be reconciled with their much older U-Pb isochron ages; i.e., these samples must have gained U from their environment recently. These gave a mean $^{234}U/^{238}U$ of 1.08 ± 0.17 and did not replicate where two of these were from the same tooth. The remaining three samples fell to the right of the infinite age U-Th isochron, i.e., have recently lost U to their surroundings. These gave a mean $^{234}U/^{238}U$ of 0.97. The U-Th analyses made on aliquots of the 2–3 mg powder samples could not be tested in this way, but replicated well on individual teeth and gave a mean $^{234}U/^{238}U$ of 1.0045 ± 0.0071 (2 s.d.). The $^{234}U/^{238}U$ values of samples which have gained or lost uranium are consistent with enhanced mobility of $^{234}U$ formed in alpha-recoil-damaged sites in the hydroxyapatite lattice.

The samples analyzed for $^{234}U/^{238}U$ and $^{230}Th/^{238}U$ are all from teeth which returned coherent U-Pb isochrons, i.e., conforming to an 'early uptake' model in which U is accumulated in dentine shortly after burial and remains unchanged thereafter. A subset of the $^{234}U/^{238}U$-$^{230}Th/^{238}U$ measurements are also consistent with U content having remained unchanged to the present day. The perturbation of the $^{234}U/^{238}U$-$^{230}Th/^{238}U$ system seen in the other samples analyzed indicates U mobility late in the burial time of the samples, perhaps reflecting enhanced groundwater interaction during exhumation. The much greater scatter of $^{234}U/^{238}U$ seen in ~75 ug samples relative to 2–3 mg samples of the same teeth indicates micro-scale heterogeneity in U mobility. Large samples giving the same mean $^{234}U/^{238}U$ as a subset of small samples that do not show U mobility indicates that U mobility is predominantly within each tooth rather than between the teeth and their environment. While such internal U mobility might increase the scatter about a U-Pb isochron, and thus reduce its calculated precision, it is unlikely to affect its accuracy to the extent that external migration might.

The U–Pb isochron age calculations include an allowance for the effect of initial disequilibrium in the U-series decay chain, here using the observed range of reliable present-day $^{234}U/^{238}U$ measurements of 1.0039 ± 0.0035.

Supplementary Note 7: Stable Isotope Discussion

Horses, which are obligate drinkers (water dependent), take most of their water from springs, rivers, or lakes, each of these sources being defined by their own isotopic drivers such as seasonality of recharge, evaporation, mixing, or recharge altitude. Rivers have lower amplitude of isotopic variability than rainfall, as they drain aquifers that are most of the time well mixed throughout the year. It is also not uncommon for rivers to show a delay of the winter signal of several months due to the input of water originating from delayed snow melt during spring but which possesses the isotopic signature of full winter conditions[18]. Nagavciuc et al.[19] present $\delta^{18}O$ data from rainwater and rivers from eastern Romania, where rainfall water has a $\delta^{18}O$ amplitude of ~10‰ with a clear seasonal signal, while rivers in the same region have amplitudes of only 1-2‰. A similar situation is encountered in southern Romania, where apart from the small amplitude in isotope values, the data of [20] show there are isotopic differences between individual rivers, depending on the extent and mean altitude of their catchments. In their study, the Olt, a major river with mountain tributaries, has lower values than its small tributaries originating in the Subcarpathians, at lower altitudes. Lakes, on the other hand, are subjected to evaporation[21] or various degrees of mixing and usually offer a more local view of isotope dynamics. As the oxygen in drinking water enters the metabolism, its $\delta^{18}O$ values suffer a range of modifications

before it is incorporated into the enamel and while the enamel matures. The effects of these processes are the smoothing of the isotopic variability inherited from drinking water, as well as an induced lag of several months[22,23].

When constructing isotope time series from the dentition of horses, the emergence and mineralization timing of individual teeth need to be known and prior studies (e.g., [24]) show that in extant horses the sequence is M1-M2-P2-P3-P4-M3, with M1 mineralizing during nursing and erupting shortly after, while M2 starts mineralizing during the last months of nursing. The $\delta^{18}O$ values we observe (Supplementary Data 3) here vary between 19.9‰ and 26.2‰ (VSMOW), with an average value of 23.5‰. Curran et al.[25] reported mean $\delta^{18}O$ values from this site between 18.9‰ to 25.3‰ (VSMOW) with an average of 21.8‰, but their values were measured on bulk samples from multiple artiodactyl specimens, incorporating enamel with an undetermined seasonal bias. Such difference in average values may also result from differences in feeding and migratory habits of these taxa, or because the incorporation of environmental signals into their enamel might be subjected to damping and lag processes of different strength. In Fig. 4 we adjusted the length of the X axis of each tooth in order to have data equally spread across one year, as defined by one summer peak value to the next peak. This allowed us to see that teeth had slightly different mineralization speeds, the highest contrast being seen for the M2, which formed at a very high rate compared to all other teeth. One could also speculate that the P2 formed at the same time and at the same rate as the M2, while the M3 might have formed at the same time as the M1, but such a claim needs to be supported by multiple similar measurements from individuals of the same species from the same site and time period.

Meteoric water $\delta^{18}O$ reconstructed from the enamel $\delta^{18}O$ of the $P^2$-$P^3$-$P^4$-$M^3$ tooth series has values between -16.3‰ and -7.8‰ (using the equation of Huertas et al. [26]). The equations of Kohn and Cerling[22] and Amiot et al.[27] result in values between -13.3‰ and -6.6‰, and -14.2‰ and -7.5‰, respectively. Across all three equations, the winter average is -14.6‰ and the summer isotopic average is -7.3‰. These results are within the bounds of variability of present-day rainfall $\delta^{18}O$ in the region (Dumbrava[28]; Isverna[29]; Cloșani and Râmnicu Vâlcea GNIP stations[30]). At Râmnicu Vâlcea, multi-annual meteoric water $\delta^{18}O$ correlates strongly with air temperature ($r=0.8$, p-value$<0.05$) and seasonal average $\delta^{18}O$ values between -14.1‰ and -3.9‰ correspond to seasonal average temperatures between -1°C and 24°C. Thus, while winter isotopic values for Grăunceanu are similar to modern day values, summer values for Grăunceanu are considerably lower.

Nevertheless, when calculating annual average values of rainfall for each tooth using the Huertas et al.[26] equation, we find the following values: -11.0‰, -12.0‰, -12.6‰, and -11.7‰ (VSMOW), while the Kohn and Cerling[22] and Amiot et al.[27] give slightly higher values. The average of annual values across the $P^2$-$P^3$-$P^4$-$M^3$ tooth series and across the three equations used above is -10.8‰ (VSMOW), lower than the present-day weighted mean at Râmnicu Vâlcea of -8.1‰. Such a large difference would result in annual temperature reconstructions of ~4°C if the equations of Rozanski et al.[31] or Pryor et al.[32] were employed and would not reconcile with the presence of warm-adapted fauna at Grăunceanu. A more likely cause of these low values might be a strong seasonal bias in precipitation, with increased precipitation in winter and decreased precipitation in summer, as compared to the modern period. In what concerns reconstruction of air temperature based on meteoric water $\delta^{18}O$, we can only state that winter temperatures might

have been similar to today. Less understood hydrological characteristics such as air mass origin, rain out history, global ice volume or moisture recycling prevent us from calculating seasonal temperatures.

Plant tissue $\delta^{13}C$ reconstructed from enamel $\delta^{13}C$ values varies between -28.9 ±0.5‰ and -25.7 ±0.5‰ (VPDB), which is consistent with feeding in a woodland to woodland-mesic C3 grassland (as defined by [33]), and supports prior environmental reconstructions for Grăunceanu[25]. The 0.5‰ uncertainty assigned to our values results from the application of the equation defining the isotopic enrichment between diet and enamel of Cerling and Harris[34], which is 14.1 ±0.5‰. The highest values are recorded in summer, which could be related to photosynthesis under drought stress[35], and the lowest values are recorded in winter (Fig. 4). Using these values and Kohn[35]'s equation to estimate total annual precipitation, we can calculate hypothetical precipitation amounts for our most extreme data points. Our lowest value of -28.9 ±0.5‰ (VPDB) translates into total precipitation between 1077 and 1775 mm/year, and our highest value of -25.7 ±0.5‰ (VPDB) equates to 70 and 258mm/year. Divided across 12 months this yields estimates of 6-22 mm for the driest (summer) month and 90-148 mm for the wettest (winter) month. If we consider an uncertainty[36] of 50% for annual values >500 mm, our MAP estimates for the wettest hypothetical year would range between 538 and 2663 mm. This further translates into a range of values for the wettest month defined as 45-222 mm. On the other hand, if we consider an uncertainty of 120 mm for the driest hypothetical year, we obtain values between -50 mm and 378 mm, which further give values for the driest month between -4 mm and 32 mm. After taking into account all available uncertainties, the driest and wettest month values do not overlap, supporting the scenario of a wet winter/dry summer climate.

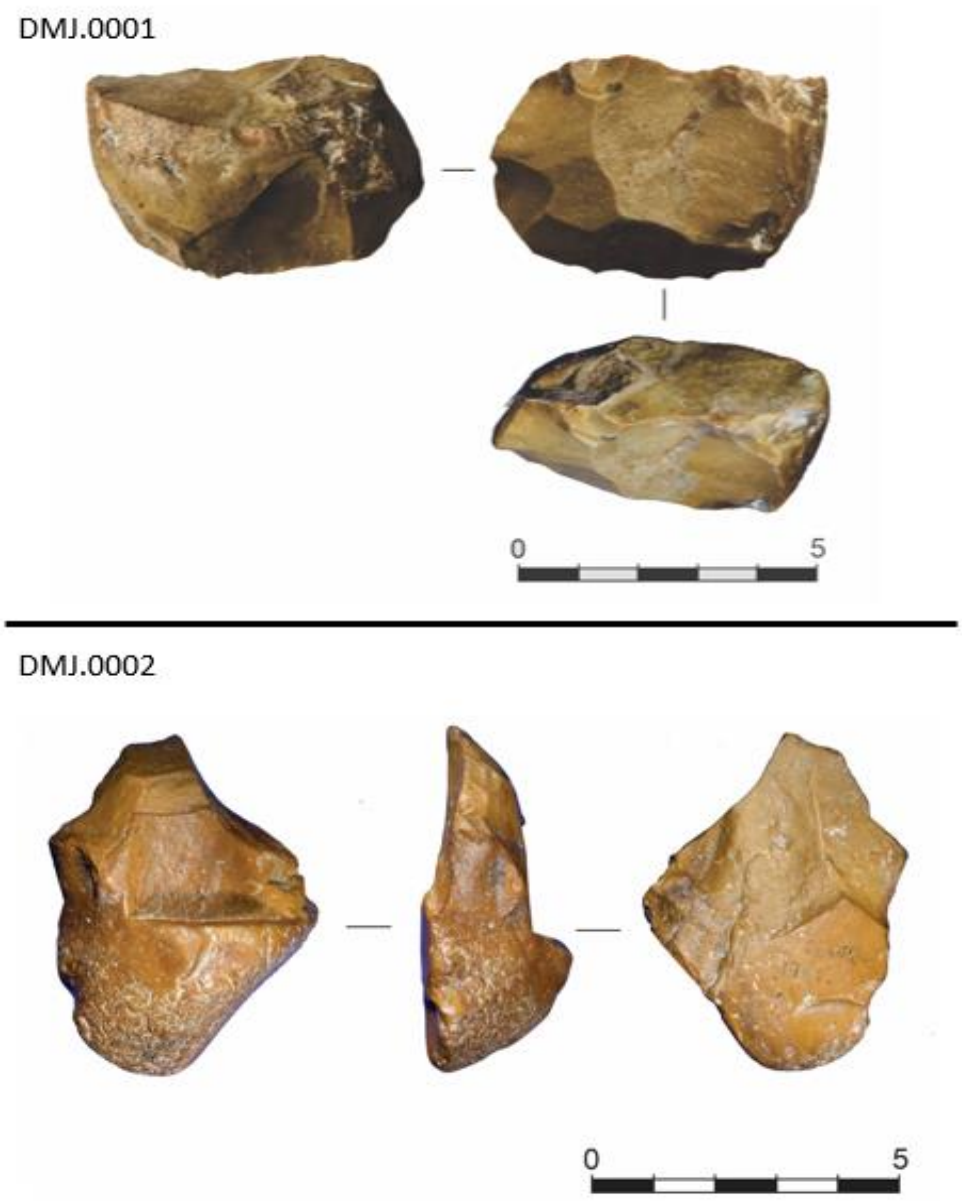


**Supplementary Fig. 1.** Lithics previously recovered from the Olteţ River Valley site of Dealul Mijlociu. Scale bar= 5 cm.

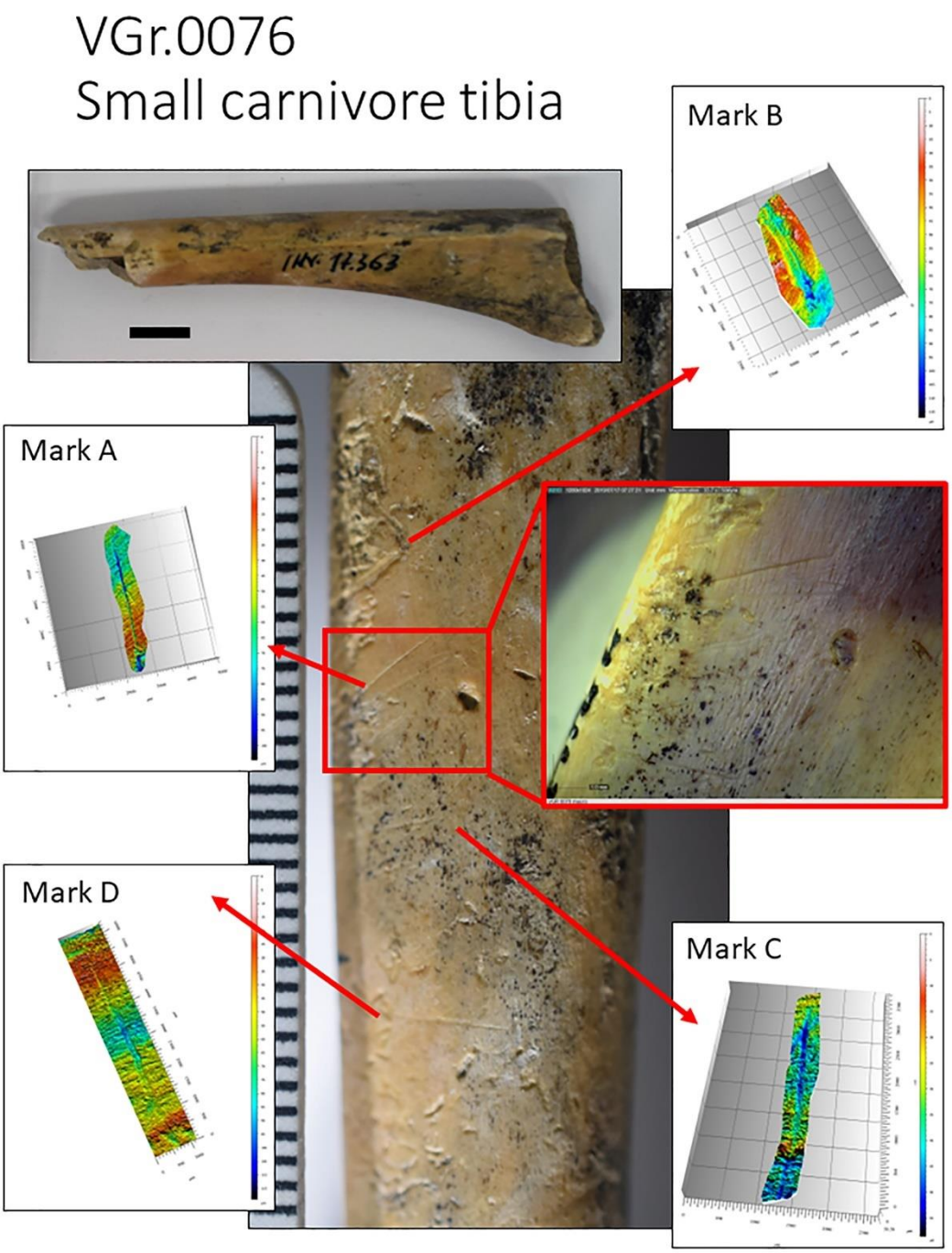


**Supplementary Fig. 2.** Photographic images and 3D models generated via profilometer showing specimen VGr.0076 that exhibits two high-confidence cut marks (marks A and C) and two probable cut marks (marks B and D).

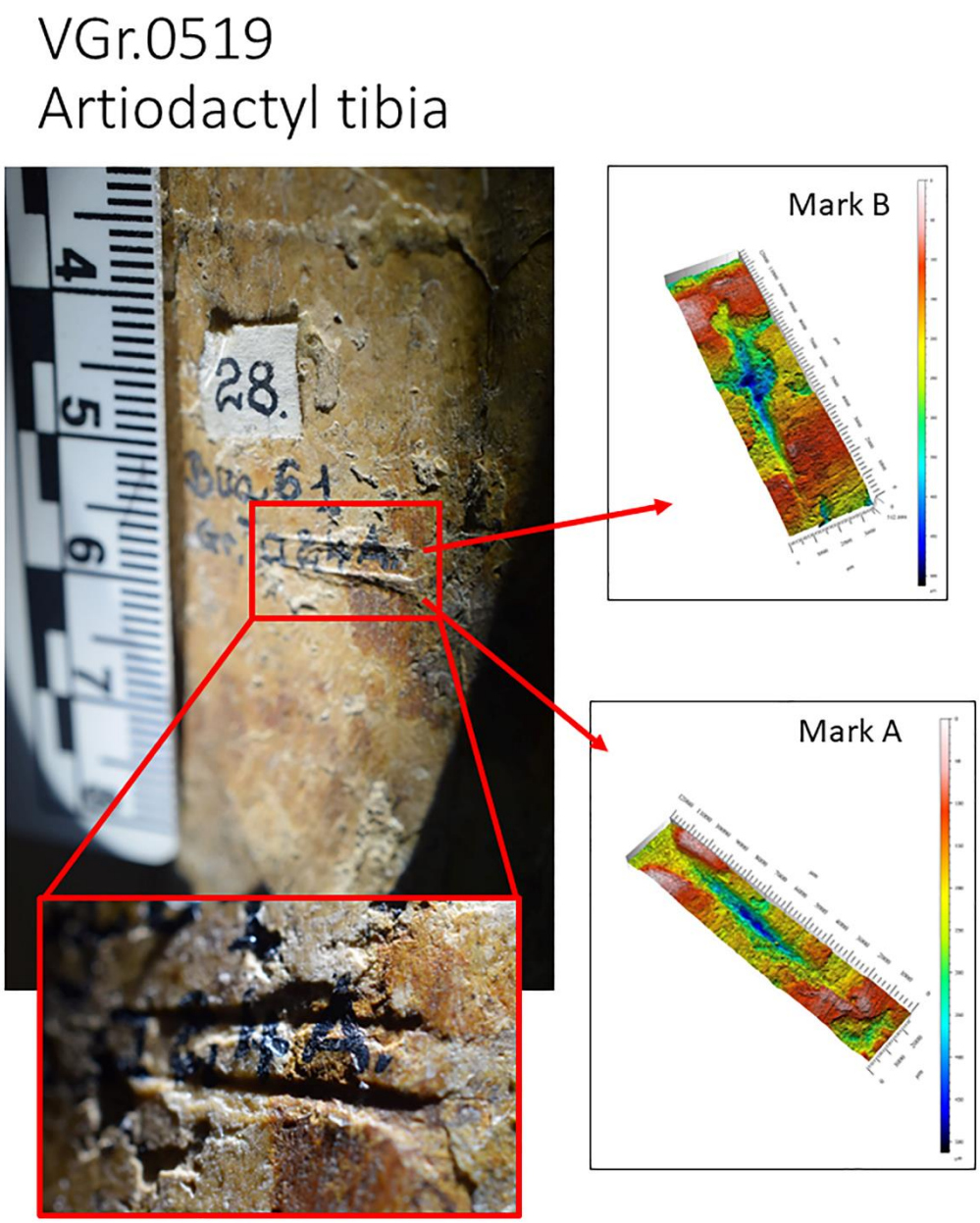


**Supplementary Fig. 3.** Photographic images and 3D models generated via profilometer showing specimen VGr.0519 that exhibits two high-confidence cut marks.

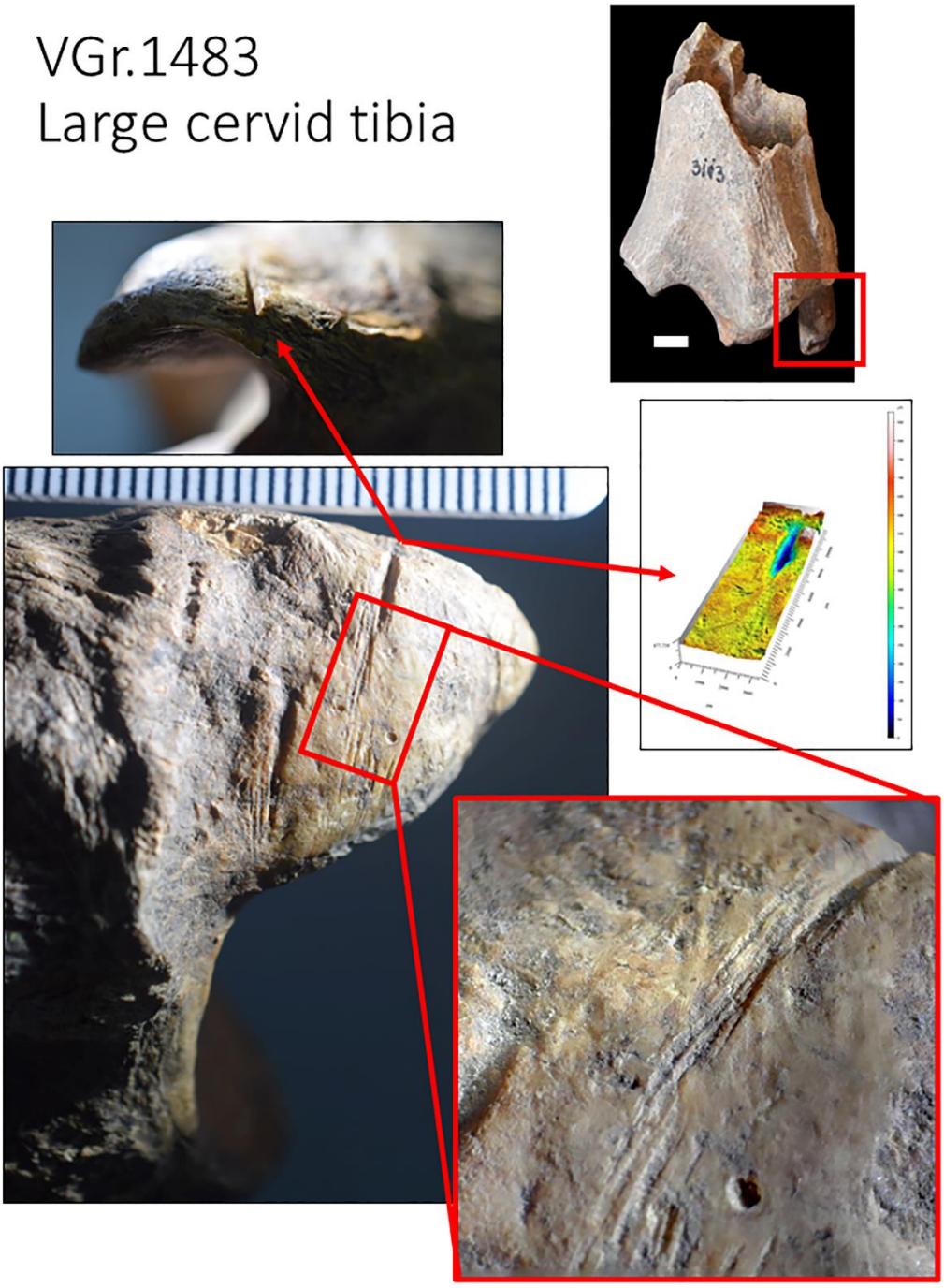


**Supplementary Fig. 4.** Photographic images and 3D models generated via profilometer showing specimen VGr.1483 that exhibits high-confidence cut marks.

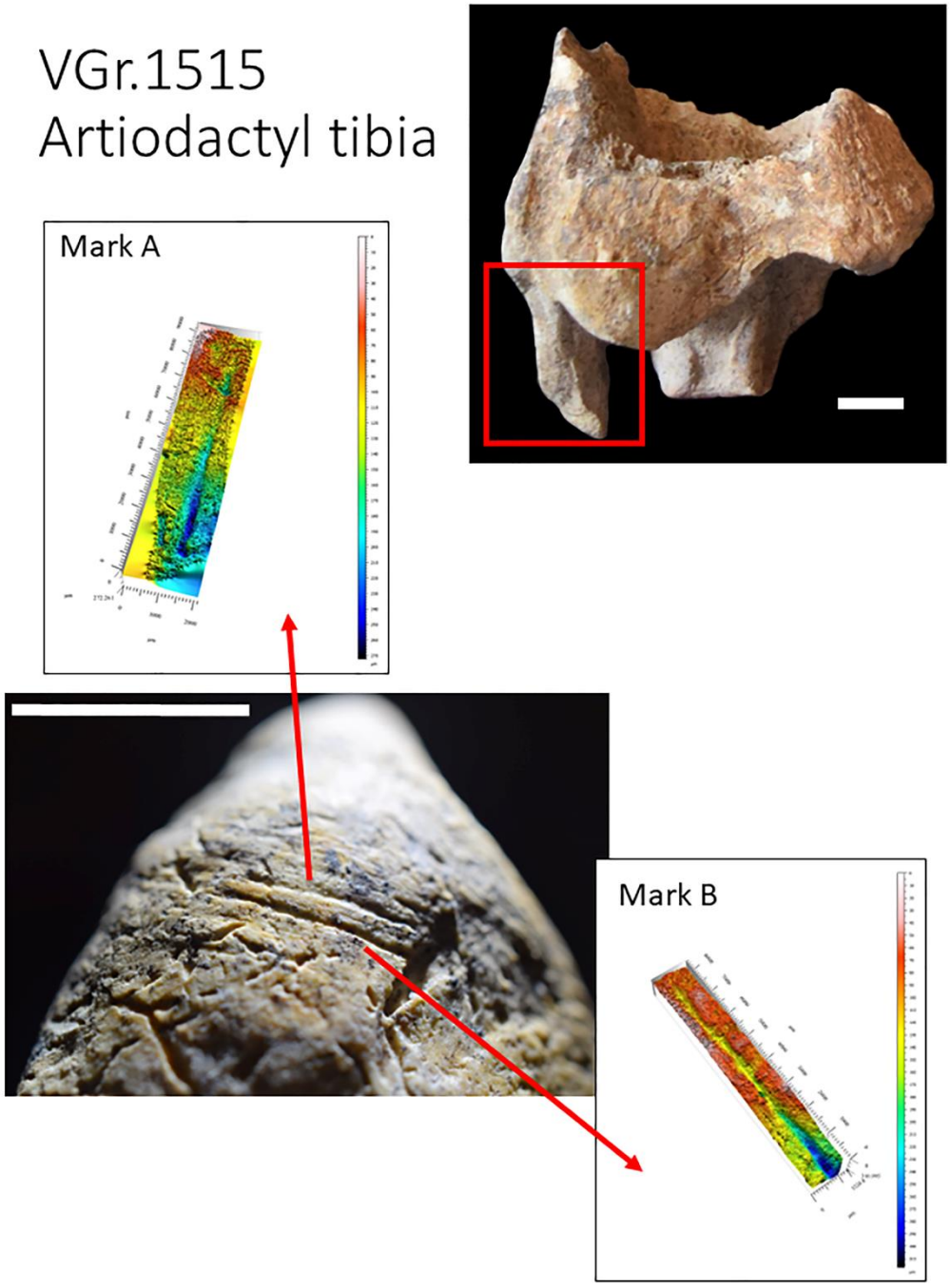


**Supplementary Fig. 5.** Photographic images and 3D models generated via profilometer showing specimen VGr.1515 that exhibits two high-confidence cut marks.

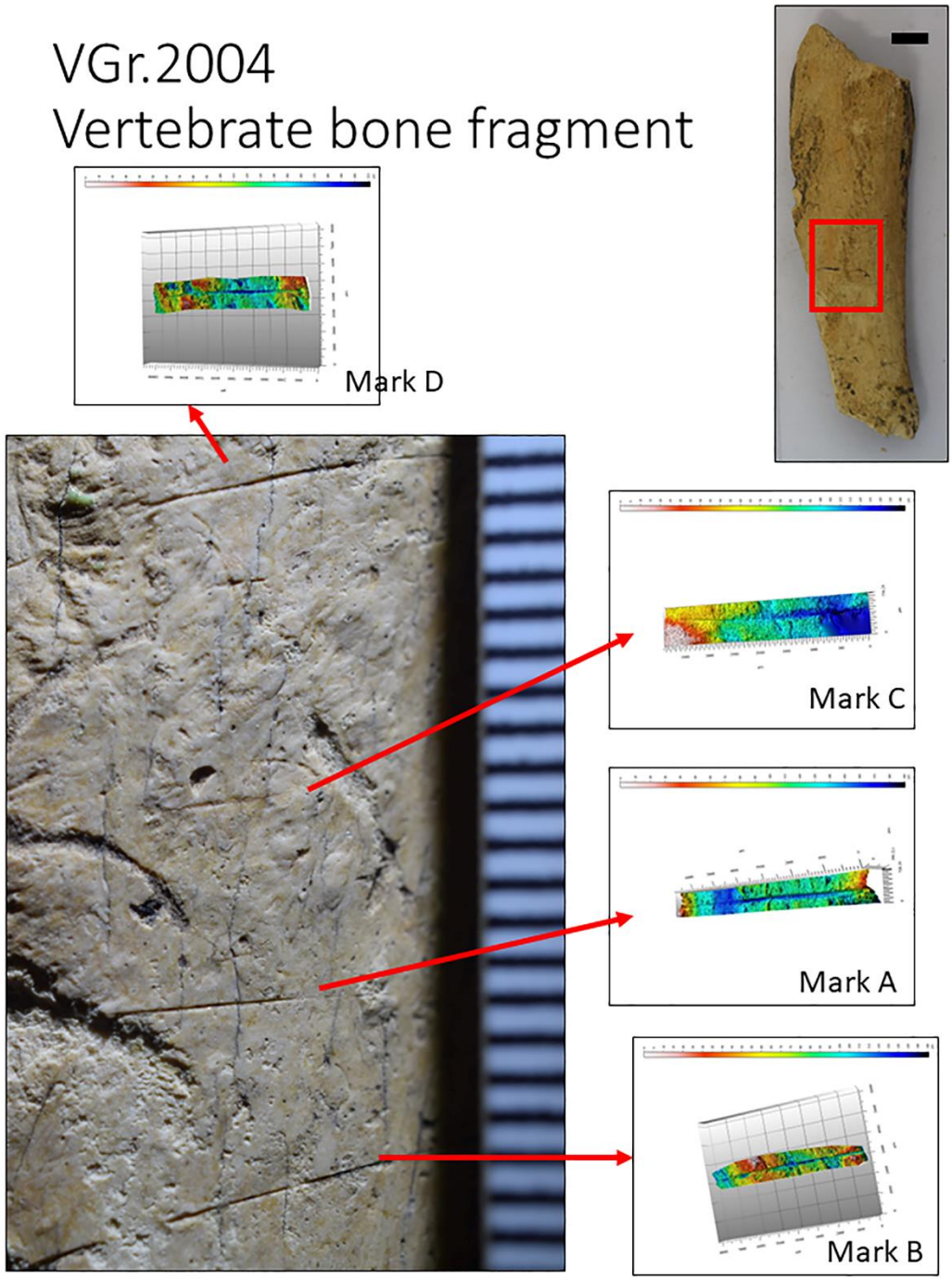


**Supplementary Fig. 6.** Photographic images and 3D models generated via profilometer showing specimen VGr.2004 that exhibits high-confidence cut marks.

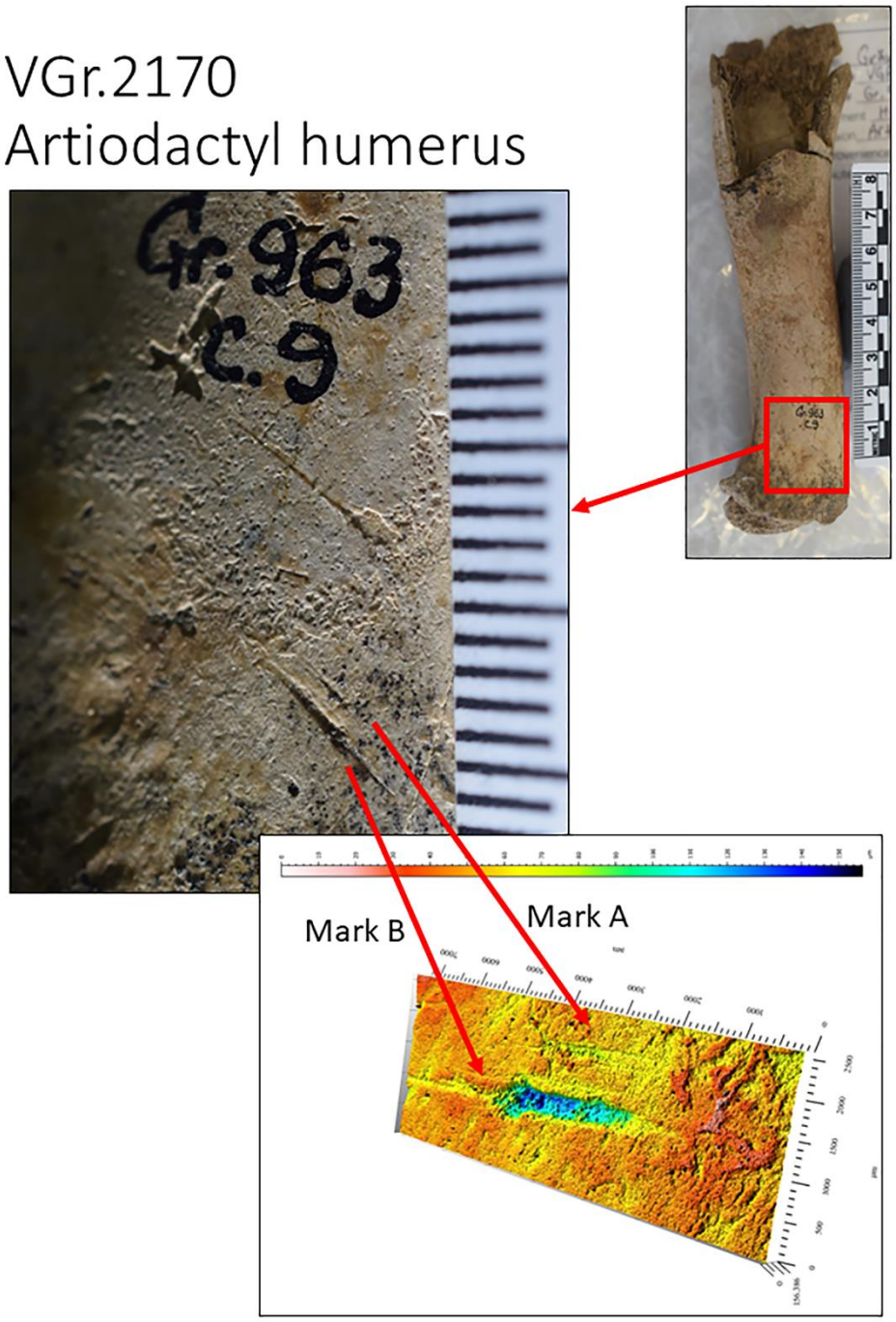


**Supplementary Fig. 7.** Photographic images and 3D models generated via profilometer showing specimen VGr.2170 that exhibits high-confidence cut marks.

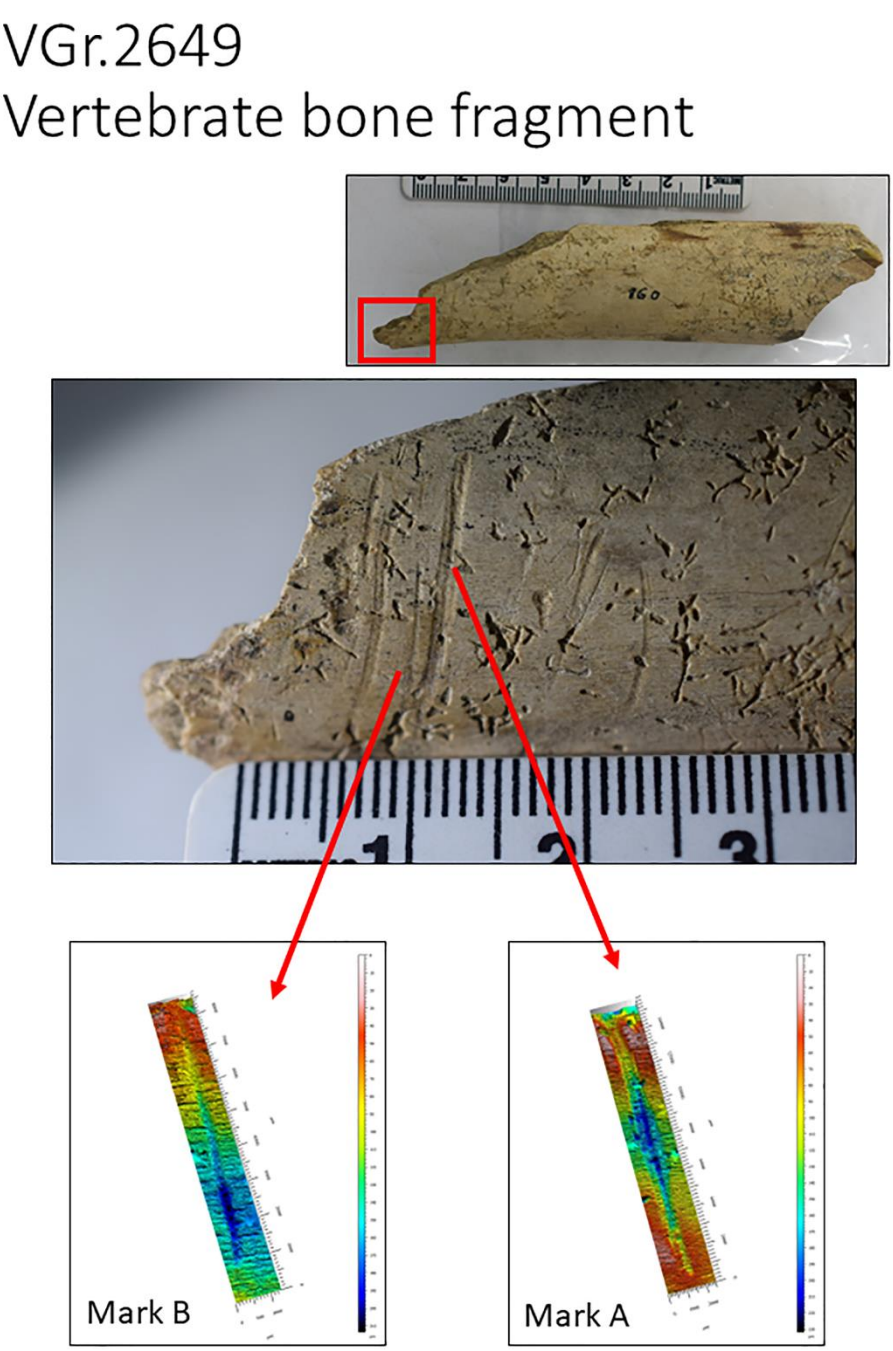


**Supplementary Fig. 8.** Photographic images and 3D models generated via profilometer showing specimen VGr.2649 that exhibits one high-confidence cut mark (mark B) and one unknown mark (mark A).

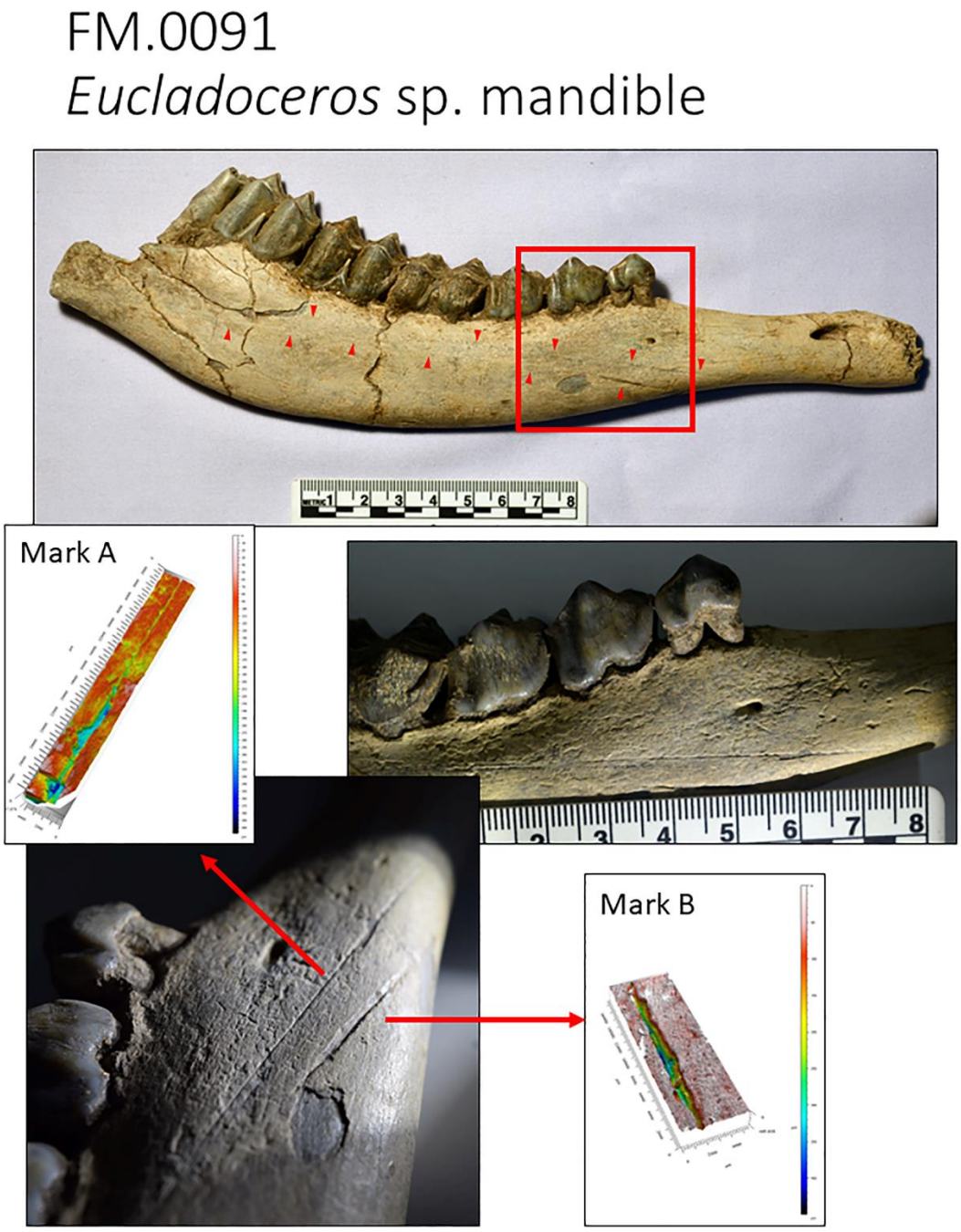


**Supplementary Fig. 9.** Photographic images and 3D models generated via profilometer showing specimen FM.0091 that exhibits two high-confidence cut marks.

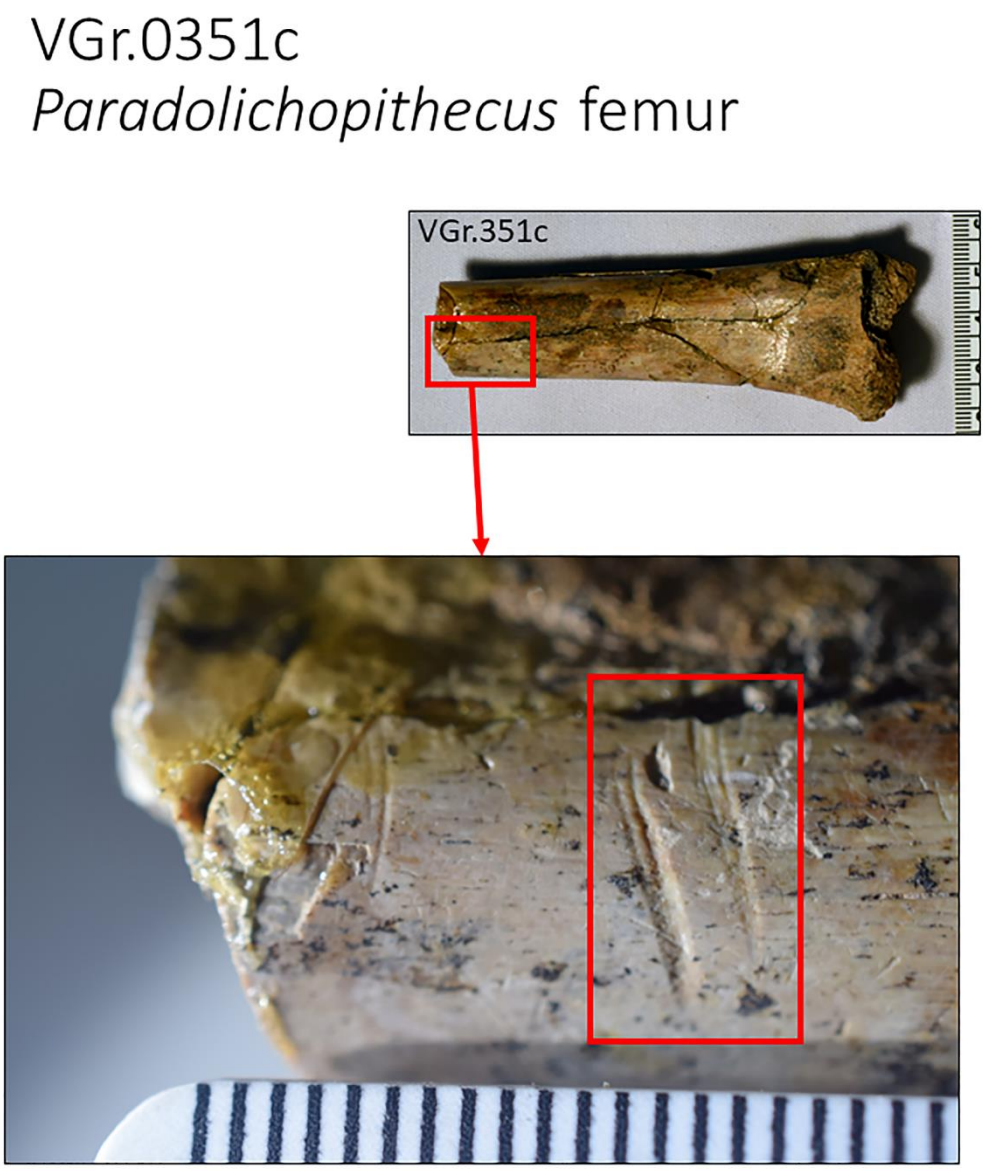


**Supplementary Fig. 10.** Photographic images showing specimen VGr.0351c that exhibits probable cut marks.


**Supplementary Fig. 11.** Photographic images and 3D models generated via profilometer showing specimen VGr.0397 that exhibits probable cut marks.

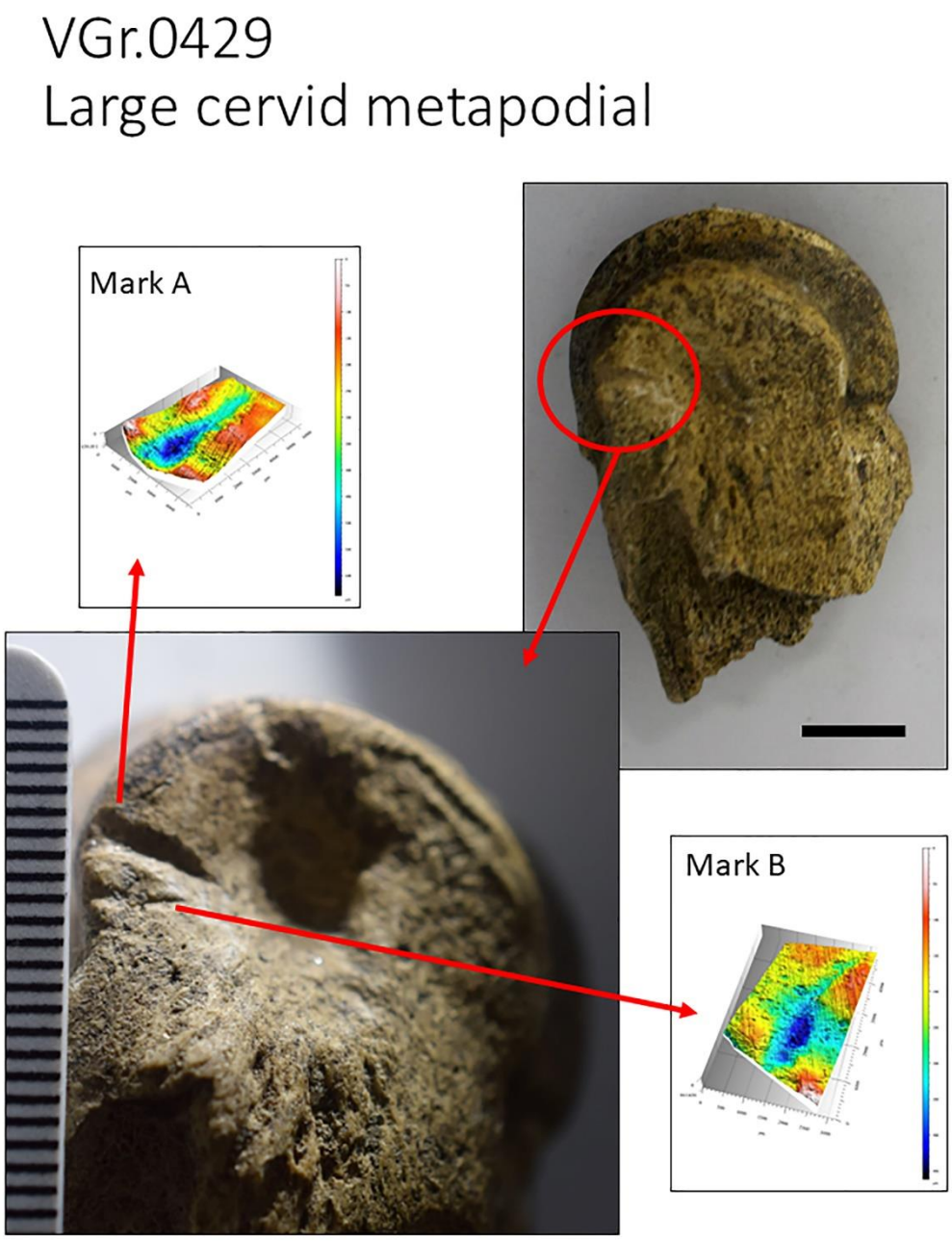


**Supplementary Fig. 12.** Photographic images and 3D models generated via profilometer showing specimen VGr.0429 that exhibits probable cut marks.

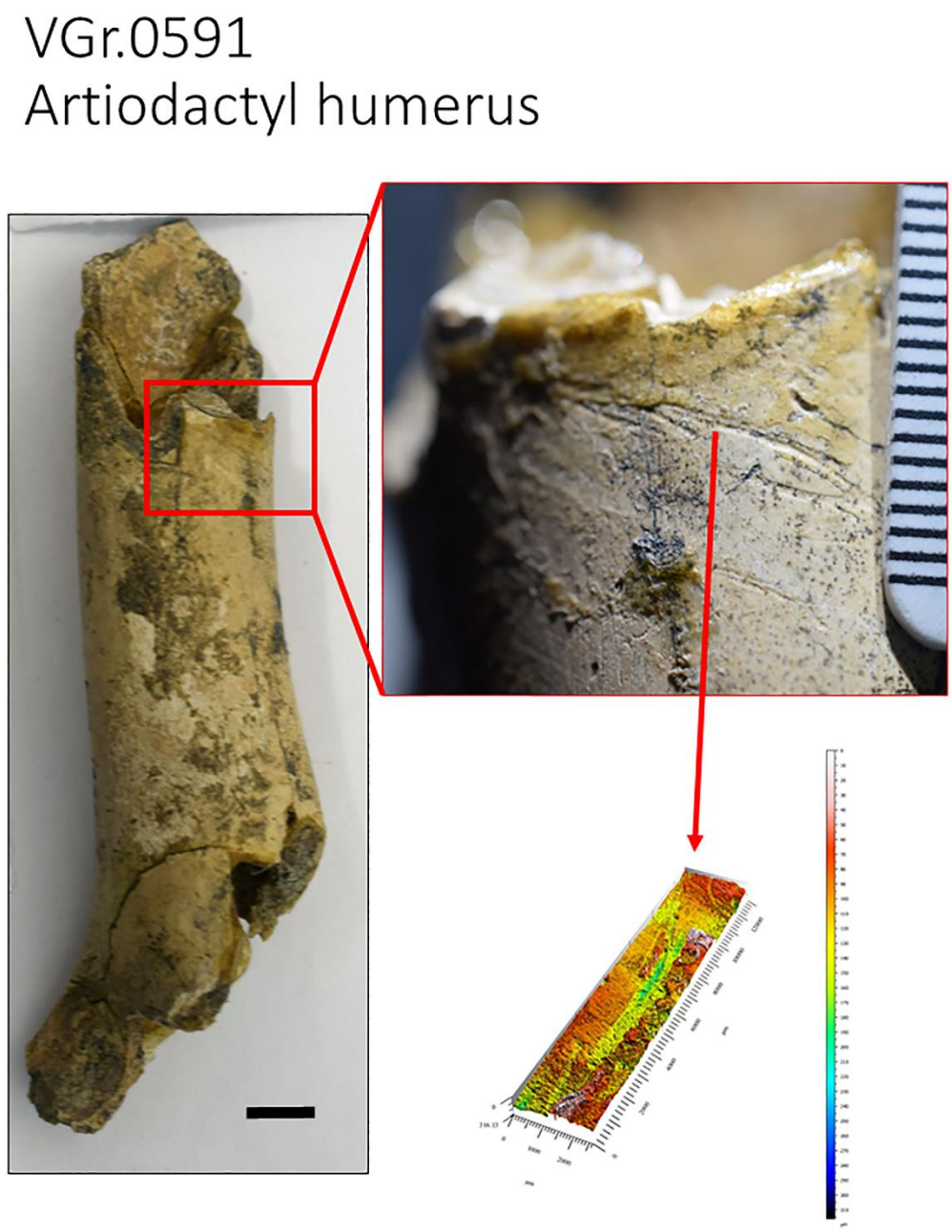


**Supplementary Fig. 13.** Photographic images and 3D models generated via profilometer showing specimen VGr.0591 that exhibits probable cut marks.


**Supplementary Fig. 14.** Photographic images and 3D models generated via profilometer showing specimen VGr.1490 that exhibits a probable cut mark.

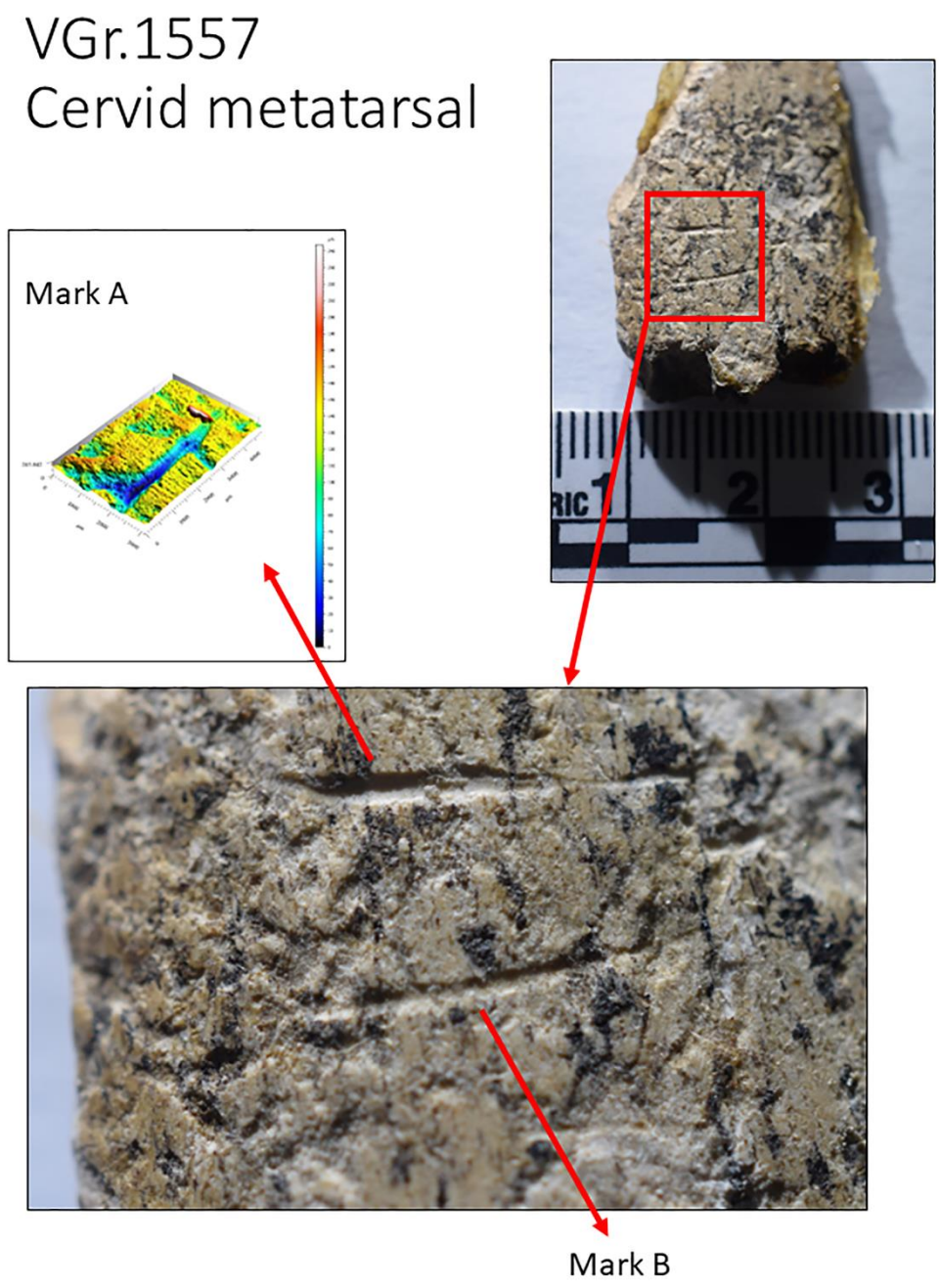


**Supplementary Fig. 15.** Photographic images and 3D models generated via profilometer showing specimen VGr.1557 that exhibits probable cut marks.

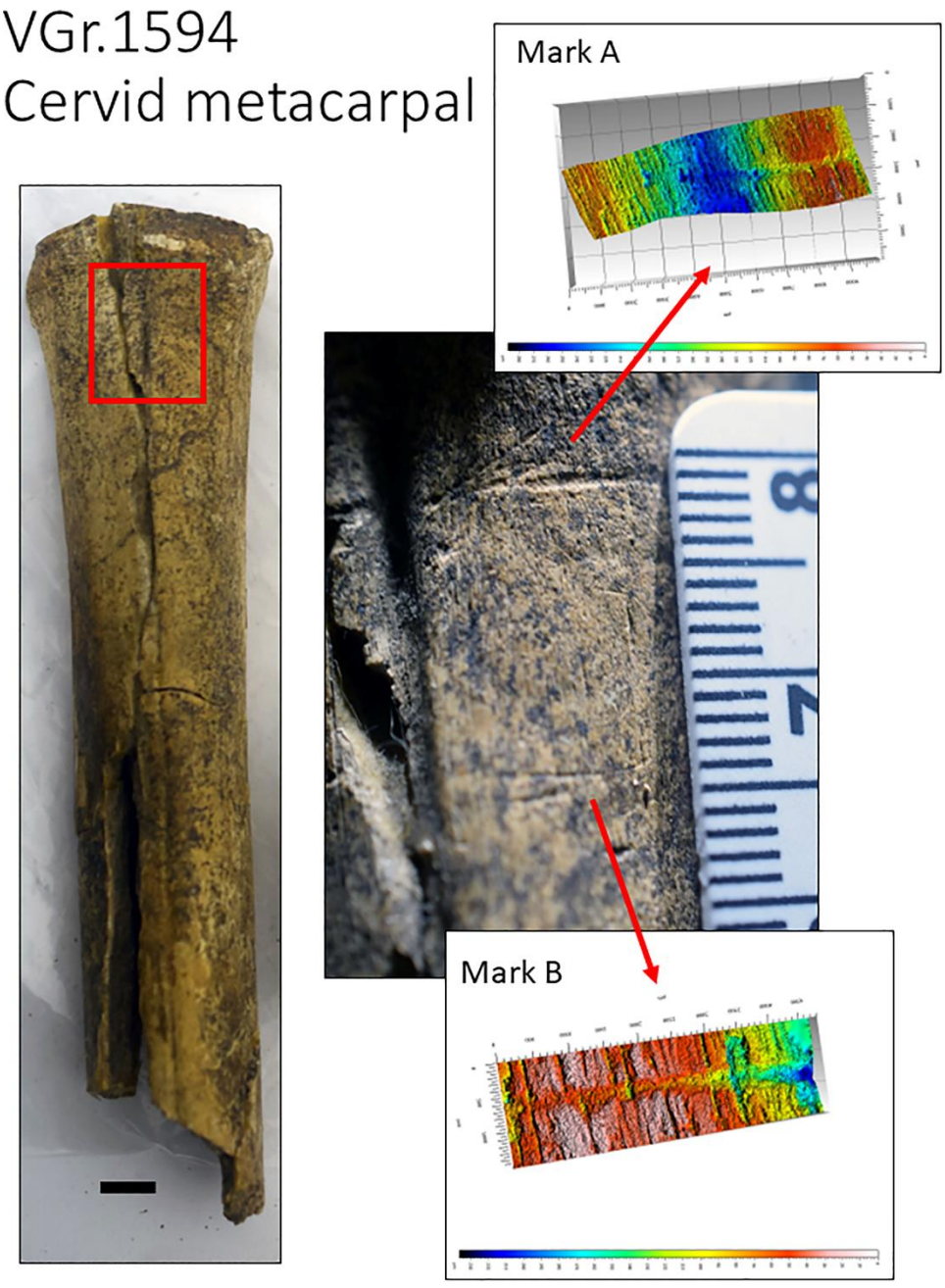


**Supplementary Fig. 16.** Photographic images and 3D models generated via profilometer showing specimen VGr.1594 that exhibits probable cut marks.

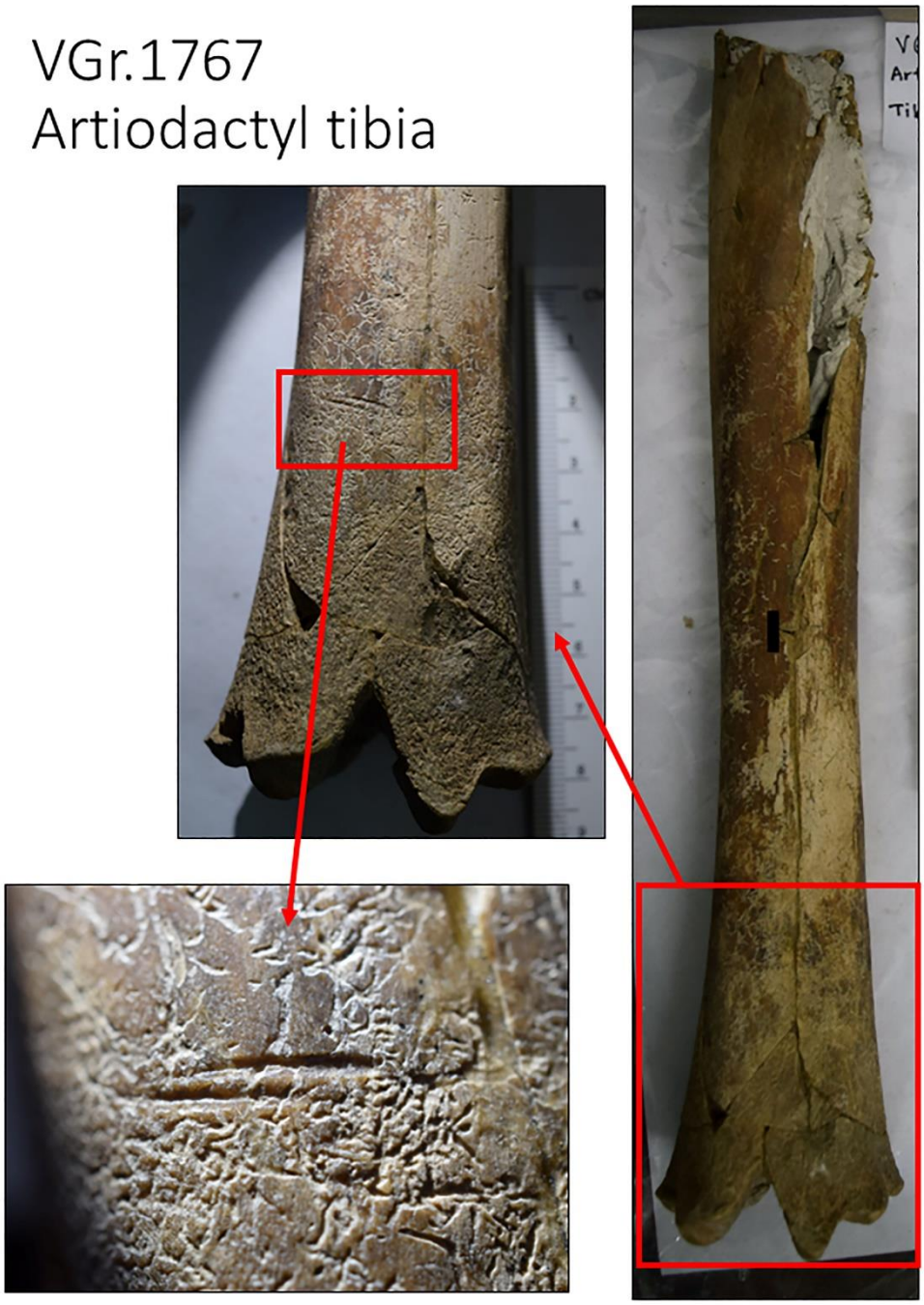


**Supplementary Fig. 17.** Photographic images showing specimen VGr.1767 that exhibits probable cut marks.

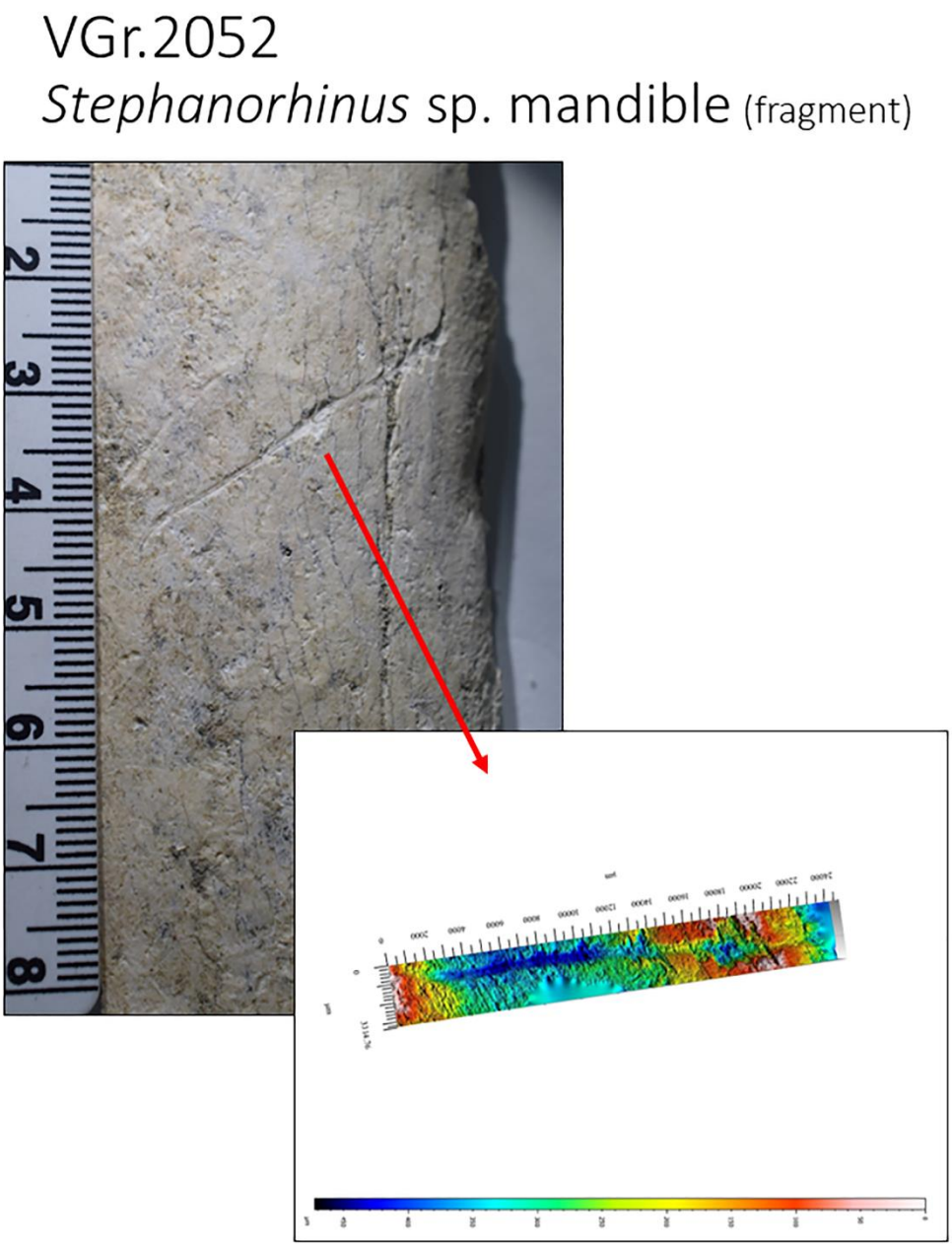


**Supplementary Fig. 18.** Photographic images and 3D models generated via profilometer showing specimen VGr.2052 that exhibits a probable cut mark.


**Supplementary Fig. 19.** Photographic images showing specimen VGr.2186 that exhibits probable cut marks.

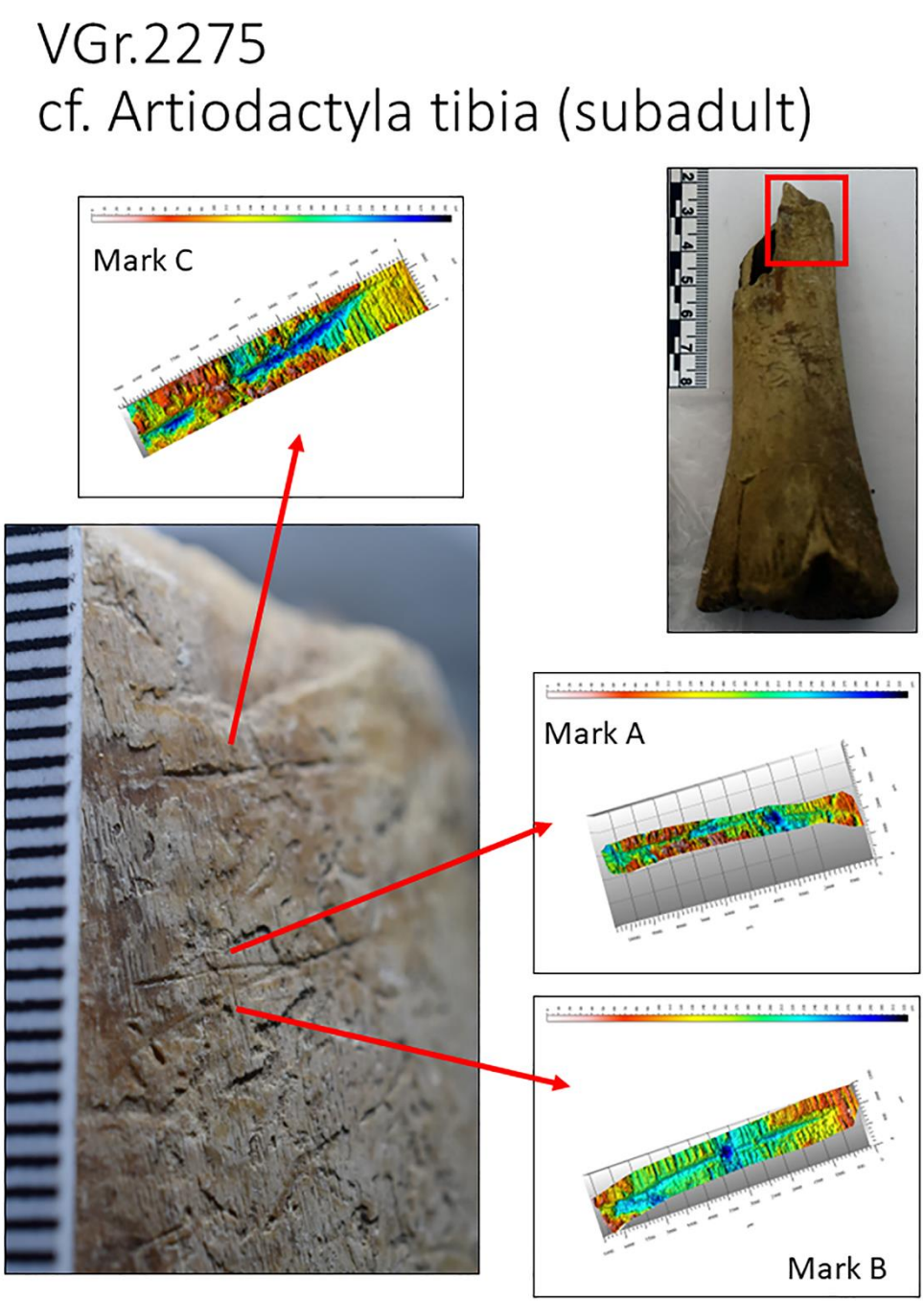


**Supplementary Fig. 20.** Photographic images and 3D models generated via profilometer showing specimen VGr.2275 that exhibits probable cut marks.

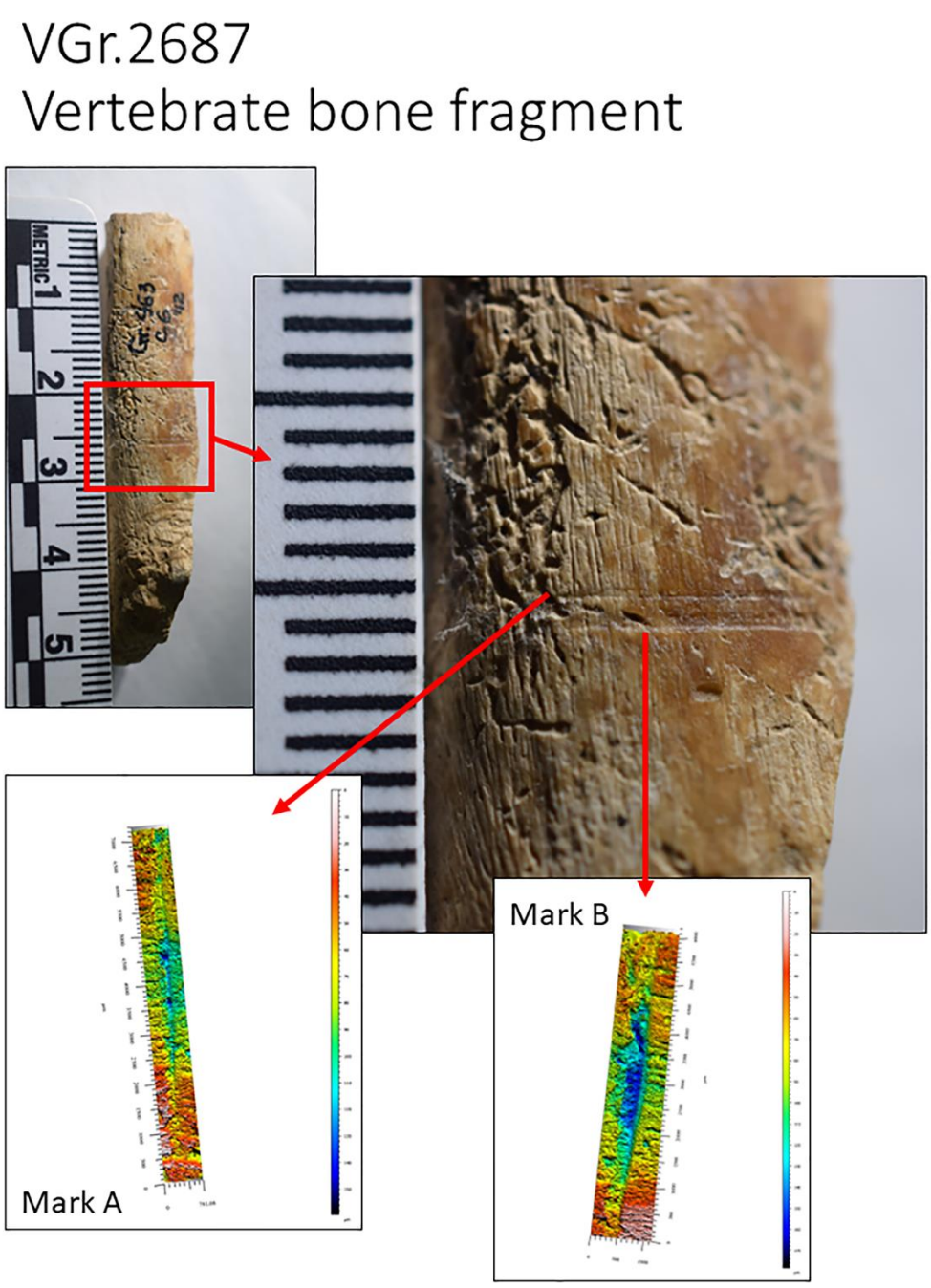


**Supplementary Fig. 21.** Photographic images and 3D models generated via profilometer showing specimen VGr.2687 that exhibits probable cut marks.

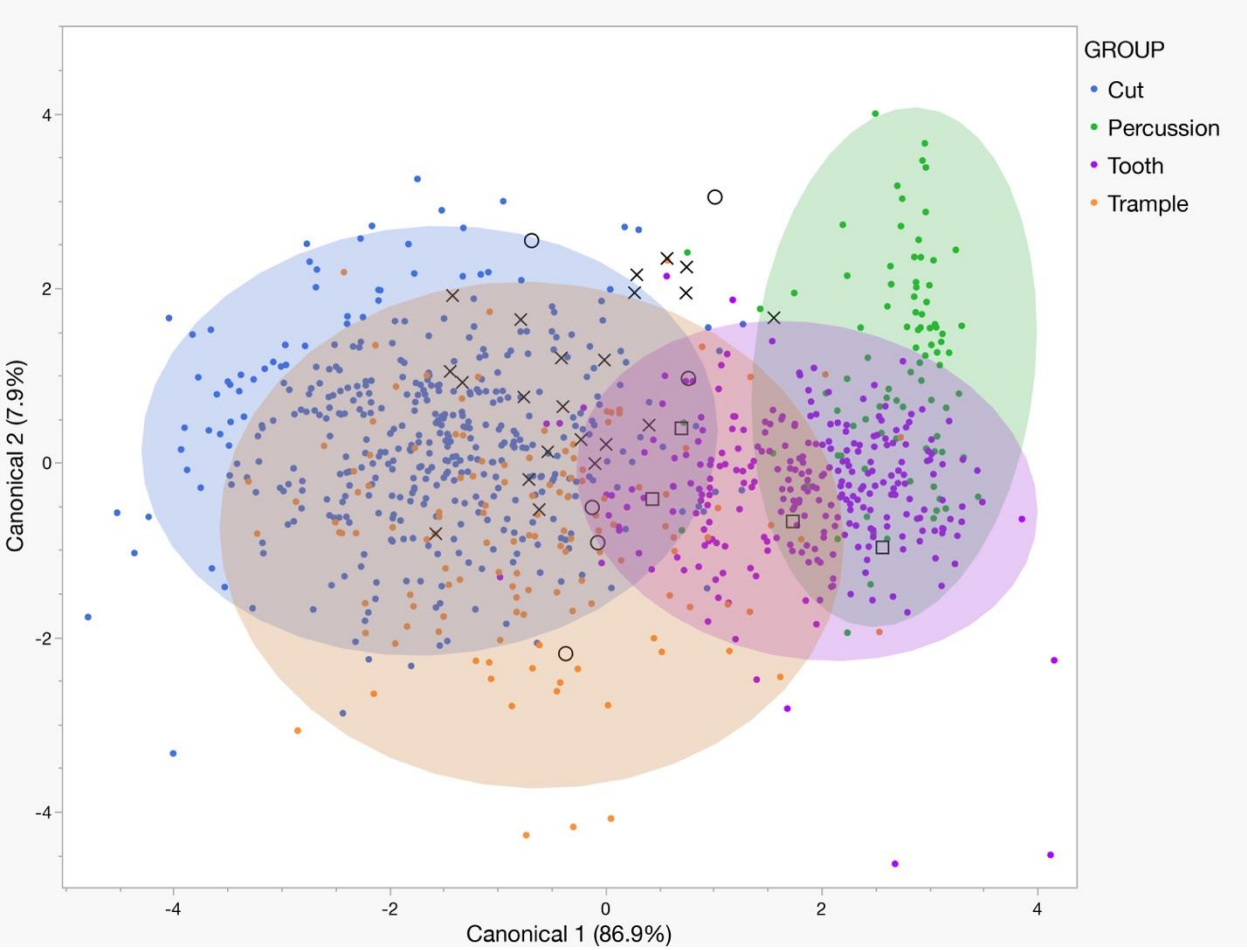


**Supplementary Fig. 22.** Results of quadratic discriminant analysis showing the individual marks in the experimental sample (n=898) and the 95% confidence intervals for mark type as indicated in the legend. Only the first two of three canonicals are shown. Fossil marks classified as cuts are shown as X's, while those classified as tooth and trample are shown as open squares and circles respectively.

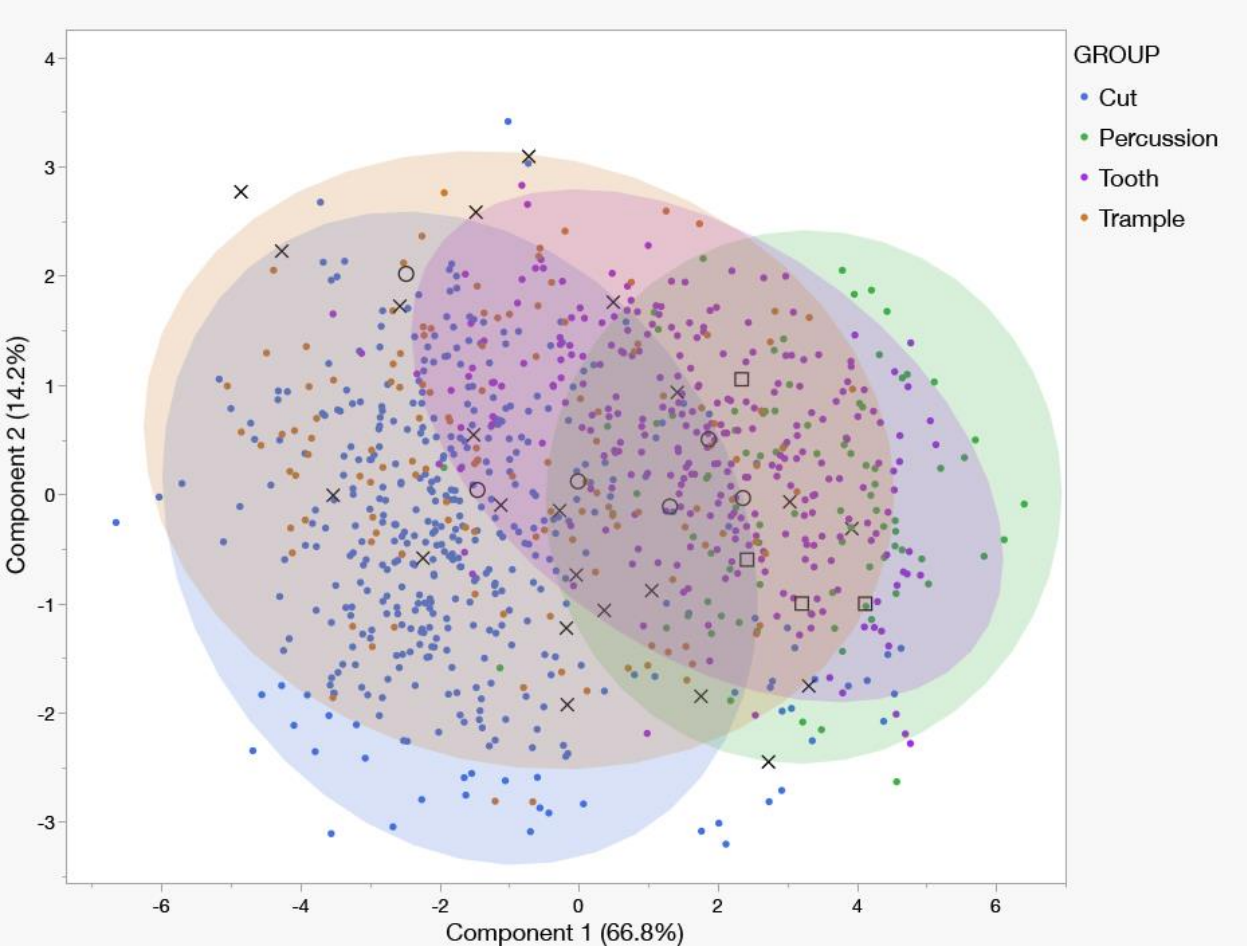


**Supplementary Fig. 23.** Principal component analysis showing the individual marks in the experimental sample (n=898) and the 95% confidence intervals for mark type as indicated in the legend. Fossil marks classified as cuts are shown as X's, while those classified as tooth and trample are shown as open squares and circles respectively.

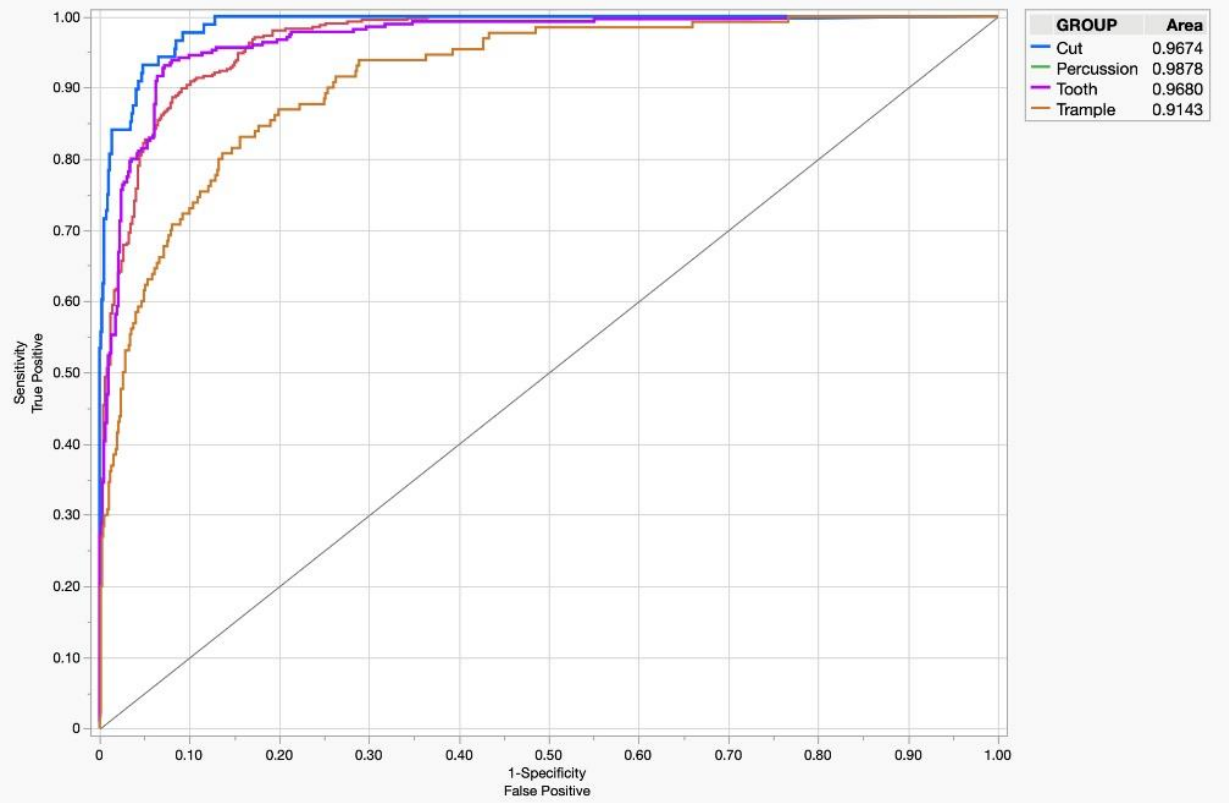


**Supplementary Fig. 24.** Receiver operating characteristic (ROC) curve for the experimental sample of bone surface modifications. Values closer to one indicate a more effective model, while those above 0.9 indicate an exceptional model. This model varies from 0.91 for predicting trample marks to 0.99 for predicting percussion marks. Results show the model is very effective at discriminating between bone surface modifications.

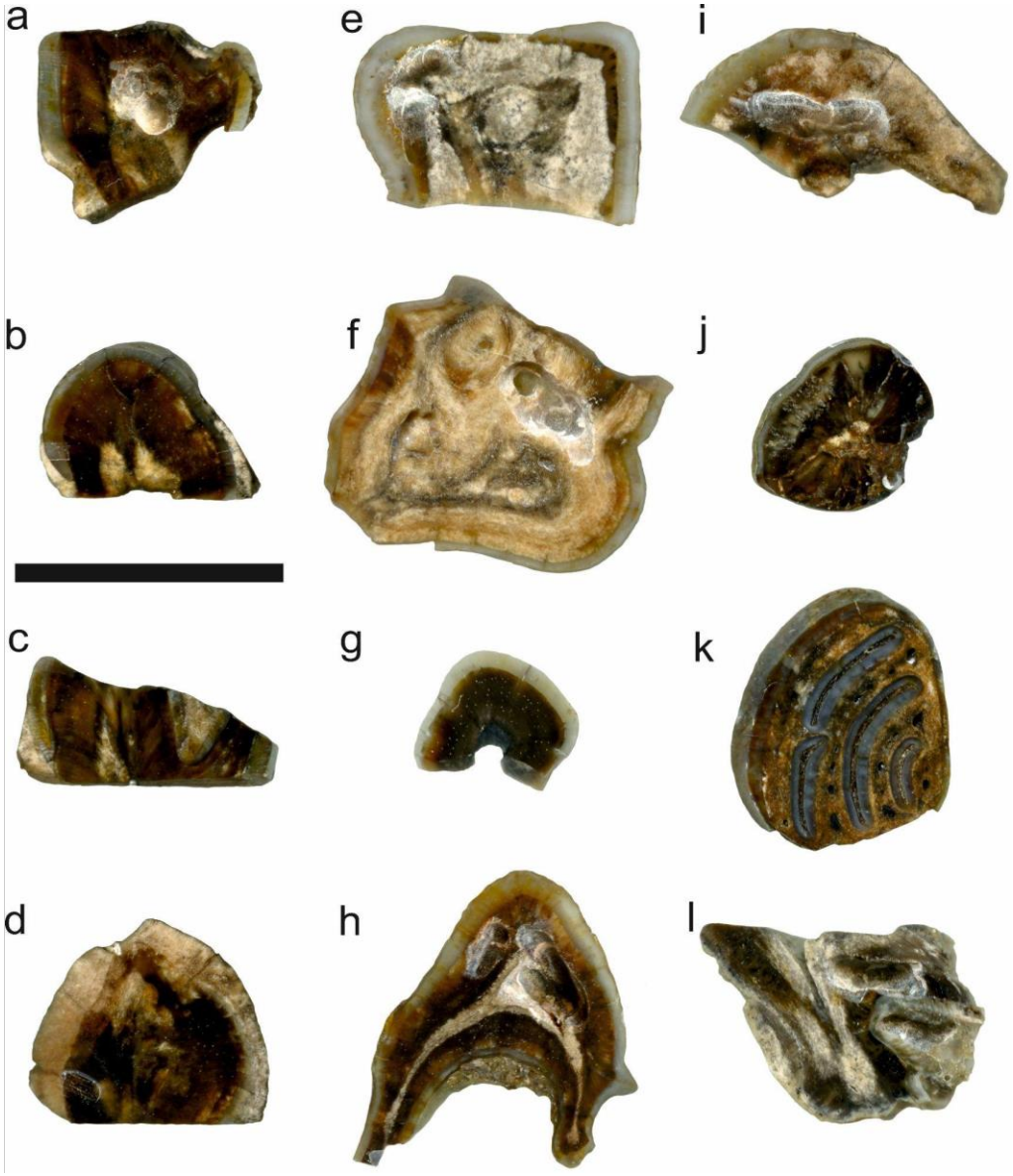


**Supplementary Fig. 25.** Tooth sections used for U-Pb dating. a. VGr.0247-A1; b. VGr.0247-A2; c. VGr.0247-B1; d. VGr.0247-B2; e. VGr.0269; f. VGr.0854; g. VGr.0870; h. VGr.0882; i. VGr.2256; j. VGr.3187; k. VRc.0001; l. FM.0019. Scale bar represents 1 cm. Drill sites for U disequilibrium measurements are visible on some specimens. Details for each specimen can be found in table S4.

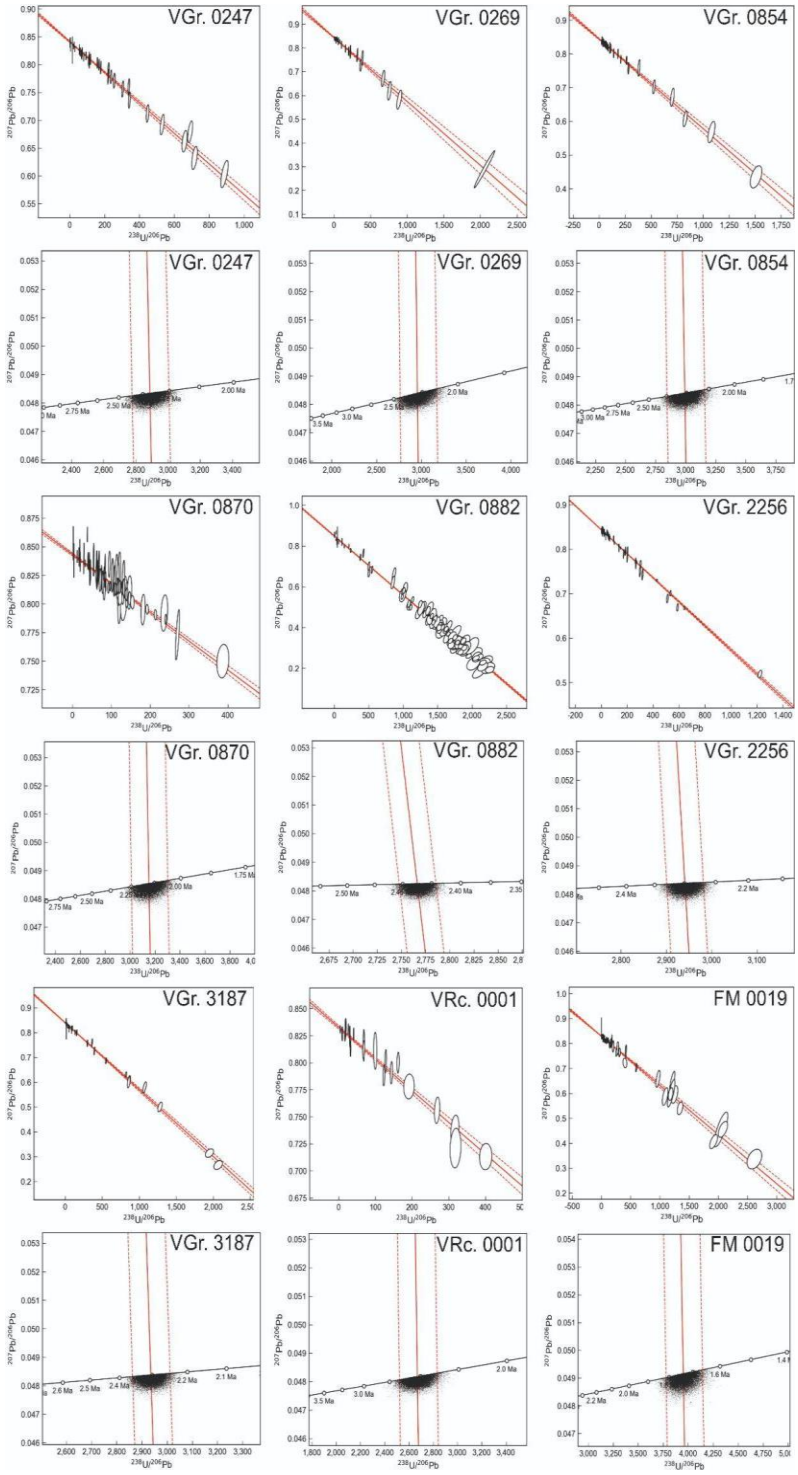


**Supplementary Fig. 26.** U-Pb isochron diagrams for the tooth samples considered in this study. The upper figure for each sample shows individual analyses with their 95% confidence ellipses, and a robust line fit (isochron) with 95% confidence uncertainty envelope calculated using [37]. The lower figure shows the intercept of the isochron with a disequilibrium concordia curve defined by a present day 234U/238U ratio of 1.0039 ± 0.0035.

**Supplementary Table 1.** Confusion matrices estimating QDA model classification accuracy with 10-fold cross-validation (top) and leave-one-out cross-validation (bottom) approaches. Models are 81.4% and 82.0% accurate, respectively, when classifying experimental bone surface modifications.

| **10-Fold Cross Validation Confusion Matrix** (Classification Accuracy = 81.4%) | | | | | | |
|---|---|---|---|---|---|---|
| | Predicted | | | | | |
| | | Cut | Percussion | Tooth | Trample | Total |
| Actual | Cut | 360 | 0 | 20 | 25 | 405 |
| | Percussion | 3 | 63 | 20 | 2 | 88 |
| | Tooth | 8 | 9 | 247 | 11 | 275 |
| | Trample | 52 | 1 | 16 | 61 | 130 |
| | | 423 | 73 | 303 | 99 | 898 |
| **Leave-One-Out Cross Validation Confusion Matrix** (Classification Accuracy = 82.0%) | | | | | | |
| | Predicted | | | | | |
| | | Cut | Percussion | Tooth | Trample | Total |
| Actual | Cut | 362 | 0 | 20 | 23 | 405 |
| | Percussion | 3 | 67 | 17 | 1 | 88 |
| | Tooth | 8 | 10 | 246 | 11 | 275 |
| | Trample | 54 | 2 | 13 | 61 | 130 |
| | Total | 427 | 79 | 296 | 99 | 898 |

**Supplementary Table 2.** Details of instrumental parameters used in the U-Pb analyses.

| **Laser ablation system** | |
|---|---|
| Manufacturer & Model | Applied Spectra RESOlution-SE |
| Ablation cell | S155 large format cell |
| Laser wavelength (nm) | 193 nm |
| Pulse width (ns) | 5 ns |
| Fluence | ~2-3 J/cm-2 |
| Repetition rate (Hz) | 5Hz |
| Spot size (mm) | 20-200 μm |
| Sampling mode / pattern | Static spot |
| Cell gases | Sample ablated into pure Helium but then rapidly (within 1cm) entrained into argon flow within the ablation volume |
| Ablation conditions | 30 seconds baseline measurement followed by 40 seconds ablation |
| Cell gas flows (l/min) | 0.27 Helium, 0.7-0.8 Argon (tuned for maximum sensitivity) |
| **ICP-MS Instrument** | |
| Make, Model & type | Nu Instruments, Attom-ES high resolution ICP-MS |
| RF power (W) | 1300 W |
| Make-up gas flow | 0.7l/min Ar |
| Detection system | Single Mascom SEM |
| Masses measured | 206, 207, 208, 232, 235, 238 |
| Integration time on peak | Dwell times of 200 μs to 2ms per peak |
| Time per cycle (secs) | 0.125 sec |
| IC Dead time (ns) | 16.5 ns |
| **Data Processing** | |
| Gas blank | 30 second on-peak zero subtracted using Iolite |
| Calibration strategy | BR-13 or McClure apatite as primary calibration standard |
| Data processing package used / Correction for LIEF | UncomPbine DRS running in Iolite provided baseline subtraction, downhole correction and calibration against the standard. The $^{207}$Pb based common Pb method was employed. |
| Uncertainty level & propagation | Ages are quoted at 2sigma absolute. Excess variance of the reference material is propagated into sample data by Iolite. |

**Supplementary Table 3.** U-Pb dating results for each of the samples analyzed in millions of years (Ma), including 95% confidence intervals. Both equilibrium ages (calculated from the original U-Pb analyses) and disequilibrium corrected ages (calculated based on $^{234}U/^{238}U$ ratios and final isochron constructions) are presented. The latter are considered the most reliable estimates of the age of these samples.

| Sample | Fossil Locality | Taxon | Equilibrium age (Ma) ±95%conf | Disequilibrium corrected age (Ma) ±2σ |
|---|---|---|---|---|
| VGr.0247 | Grăunceanu | Artiodactyl isolated incisor | 2.23±0.09 | 1.97±0.18 |
| VGr.0269 | Grăunceanu | Cervid mandibular premolar | 2.17±0.15 | 1.94±0.20 |
| VGr.0854 | Grăunceanu | Cervid mandibular molar | 2.15±0.11 | 1.93±0.09 |
| VGr.0870 | Grăunceanu | Cervid incisor | 2.04±0.09 | 1.87±0.16 |
| VGr.0882 | Grăunceanu | Cervid maxillary M3 | 2.32±0.02 | 2.01±0.20 |
| VGr.2256 | Grăunceanu | *Rucervus radulescui* maxillary M2 | 2.19±0.03 | 1.95±0.18 |
| VGr.3187 | Grăunceanu | Castorid incisor | 2.19±0.06 | 1.95±0.18 |
| VRc.0001 | Valea Roșcăi | *Trogontherium* sp. molar | 2.41±0.14 | 2.05±0.22 |
| FM.0019 | Fântâna lui Mitilan | Cervid maxillary molar | 1.63±0.07 | 1.61±0.10 |

**Supplementary Table 4.** Uranium-Thorium (U-Th) analysis results. Values in parentheses represent uncertainties (2σ) for the last two significant figures presented.

| Sample | Lab Number[a] | U(ngg-1) | $^{230}Th/^{238}U$[b] | $^{234}U/^{238}U$[b] | $^{230}Th/^{232}Th$[b] | U mobility[c] |
|---|---|---|---|---|---|---|
| VGr.0247 | MXF230531-019 | 164148 | | 1.0189(26) | | |
| VGr.0247 | MXF230602-048 | 178869 | | 1.0141(19) | | |
| VGr.0247-2 | UMF230908-228 | 152835 | 1.0016(69) | 1.0057(21) | 73281 | Closed |
| VGr.0247-3 | UMF230908-271 | 155412 | 1.0042(50) | 1.0051(21) | 135134 | Closed |
| VGr.0269 | MXF230602-046 | 130350 | | 1.0060(19) | | |
| VGr.0269 | MXF230531-017 | 111753 | | 1.0080(17) | | |
| VGr.0269-2 | UMF230908-502 | 640521 | 0.7230(30) | 1.0989(22) | 130600 | U gain |
| VGr.0269-3 | UMF230908-512 | 146848 | 0.9997(62) | 1.0036(24) | 72251 | Closed |
| VGr.0854 | MXF230602-047 | 311947 | | 1.0021(18) | | |
| VGr.0854 | MXF230531-018 | 271001 | | 1.0015(23) | | |
| VGr.0854-3 | UMF230908-440 | 326212 | 0.9992(51) | 1.0009(28) | 191022 | Closed |
| VGr.0854-4 | UMF230908-451 | 162580 | 0.9975(55) | 1.0070(24) | 41852 | U gain |
| VGr.0870-2 | UMF230908-522 | 770618 | 0.9142(34) | 0.9709(19) | 137470 | U gain |
| VGr.0870-3 | UMF230908-531 | 141100 | 0.7211(37) | 0.9035(25) | 86850 | U gain |
| VGr.0882 | MXF230602-050 | 123180 | | 1.0043(18) | | |
| VGr.0882 | MXF230531-021 | 91633 | | 1.0086(20) | | |
| VGr.0882-2 | UMF230908-306 | 184911 | 0.9995(55) | 1.0031(30) | 123016 | Closed |
| VGr.0882-3 | UMF230908-372 | 354248 | 1.0035(48) | 1.0051(17) | 196752 | Closed |
| VGr.2256 | MXF230602-049 | 1264655 | | 0.9996(19) | | |
| VGr.2256 | MXF230531-020 | | | 1.0011(19) | | |
| VGr.2256-2 | UMF230908-298 | 3339551 | 1.0083(39) | 0.9987(24) | 1171687 | U loss |
| VGr.2256-3 | UMF230908-294 | 481246 | 0.9836(37) | 1.0021(19) | 296338 | U gain |
| VGr.3187-2 | UMF230908-420 | 109633 | 0.9638(69) | 1.0292(26) | 292 | U gain |
| VGr.3187-4 | UMF230908-613 | 339211 | 0.9925(35) | 1.0085(26) | 3778 | U gain |
| VRc.0001-2 | UMF230908-374 | 250718 | 1.5057(63) | 1.4523(44) | 148454 | U gain |
| VRc.0001-3 | UMF230908-387 | 72797 | 1.4835(61) | 1.4278(32) | 59766 | U gain |
| FM.0019 | MXF230602-045 | 553689 | | 0.9943(17) | | |
| FM.0019 | MXF230531-016 | 497714 | | 0.9959(17) | | |
| FM.0019-2 | UMF230908-543 | 485015 | 0.9624(45) | 1.0054(20) | 37705 | U gain |
| FM.0019-3 | UMF230908-549 | 1820873 | 1.0455(35) | 1.0142(20) | 9369 | U loss |

[a] Samples with lab number MXF* are aliquots of a bulk dissolution of 2–3 mg of dentine, UMF* are individual 350 um drill samples

[b] Activity ratios determined at the University of Melbourne after Hellstrom (2003) and Drysdale et al (2012)

[c] inferred status of recent uranium mobility according to relationship to U-Th infinite age isochron (see text)

**Supplementary Table 5.** Percentages of cut marks reported for Early Pleistocene Eurasian and North African sites including the number of specimens and percentage of the assemblage displaying cut marks (CM), the number of identified specimens (NISP) for that assemblage, and whether a full taphonomic assessment of the entire assemblage for that site has been conducted (Full taph?).

| Site | Age (Ma) | CM% | CM# | NISP | Full taph? | Reference |
|---|---|---|---|---|---|---|
| Masol, India | 2.6 | 0.204 | 3 | 1469 | partial | [38] |
| Aïn Boucherit (Lw), Algeria | 2.4 | 5.743 | 17 | 296 | yes | [39] |
| Muhkai 2, Russia | 2.1-1.77 | 0.040 | 1 | 2498 | unclear | [40] |
| Liventsovka, Russia | 2.1-1.97 | 0.003 | 1 | 33000 | unclear | [41] |
| Grăunceanu, Romania | >1.95 | 0.176/0.442[a] | 8/20 | 4524 | yes | this study |
| Aïn Boucherit (Up), Algeria | 1.9 | 0.722 | 2 | 277 | yes | [39] |
| Dmanisi, Georgia | 1.8-1.76 | 0.392 | 30[b] | 7658 | yes | [42] |
| Trlica, Montenegro | 1.8-1.5 | 0.112 | 1 | 895 | yes | [43] |
| El Kherba, Algeria | 1.78 | 2.100 | 13 | 619 | yes | [44] |
| Pirro Nord, Italy | 1.6-1.3 | 1.089 | 14 | 1285 | yes | [45] |
| Bizat Ruhama, Israel | 1.6-1.2 | 0.709 | 1 | 141 | yes | [46] |
| 'Ubeidiya, Israel | 1.5-1.2 | 0.262 | 16 | 6099 | yes | [47] |
| Sangiran, Indonesia | 1.45-0.79 | 0.006 | 2[c] | 34000 | unclear | [48] |
| Barranco León, Spain | 1.4 | 0.753 | 32 | 4249[d] | yes | [49] |
| Bois-de-Riquet, France | 1.3-1.2 | 0.070 | 2 | 2875 | yes | [50] |
| Vallonnet Cave, France | 1.2-1.1 | 0.021 | 12 | 57759[e] | yes | [51,52] |
| Sima del Elefante, Spain | 1.2-1.1 | 5.000 | NR | NR | yes | [53] |
| Fuenta Nueva 3, Spain | 1.19 | 0.831 | 32 | 3852[d] | yes | [49] |

unclear = it is unclear if the authors of the relevant studies assessed taphonomy for every specimen reported as the NISP; NR= not reported

a- Numbers for Grăunceanu indicate high certainty/probable marks

b- Exact number of specimens with marks (rather than total marks) not reported

c- Reported as 18 cut marks on 2 specimens; likely made with clam shells

d- this NISP represents a subset of the larger assemblage

e- total NISP analyzed for taphonomy unclear

## References


1 Radulesco, C. & Samson, P. The Plio-Pleistocene Mammalian Succession of the Olteţ Valley, Dacic Basin, Romania. *Quartärpalaontologie* **8**, 225-232 (1990).

2 Andreescu, I. *et al.* Reassessment of the Pliocene/Pleistocene (Neogene/ Quaternary) boundary in the Dacian Basin (Eastern Paratethys), Romania. *Oltenia. Studii şi comunicări. Ştiinţele Naturii.* **27**, 197-220 (2011).

3 Andreescu, I. *et al.* New developments in the Upper Pliocene-Pleistocene stratigraphic units of the Dacian Basin (Eastern Paratethys), Romania. *Quatern Int* **284**, 15-29 (2013). https://doi.org/10.1016/j.quaint.2012.02.009

4 Radulesco, C., Samson, P.-M. & Stiuca, E. Biostratigraphic framework of the lower paleolithic in Romania. *Quaternaire* **9**, 283-290 (1998).

5 Radulescu, C. & Samson, P. in *Les Premiers Européens.* (eds E. Bonifay & B Vandermeersch) 203-207 (Éditions du C.T.H.S.).

6 Păunescu, A. Paleoliticul şi mezoliticul de pe teritoriul cuprins între Carpaţi şi Dunăre. *Bucureşti: AGIR* (2000).

7 Behrensmeyer, A. K. Taphonomic and Ecologic Information from Bone Weathering. *Paleobiology* **4**, 150-162 (1978). https://doi.org/10.1017/S0094837300005820

8 Pobiner, B., Pante, M. & Keevil, T. Early Pleistocene cut marked hominin fossil from Koobi Fora, Kenya. *Sci Rep-Uk* **13** (2023). https://doi.org/https://doi.org/10.1038/s41598-023-35702-7

9 Nilssen, P. J. *An actualistic butchery study in South Africa and its implications for reconstructing hominid strategies of carcass acquisition and butchery in the Upper Pleistocene and Plio-Pleistocene* PhD thesis, University of Cape Town, (2000).

10 Soulier, M. C. & Costamagno, S. Let the cutmarks speak! Experimental butchery to reconstruct carcass processing. *J Archaeol Sci-Rep* **11**, 782-802 (2017). https://doi.org/10.1016/j.jasrep.2016.12.033

11 Grün, R. Direct dating of human fossils. *Yearbook of Physical Anthropology, Vol. 49 2006* **49**, 2-48 (2006). https://doi.org/10.1002/ajpa.20516

12 Pike, A. W. G. & Hedges, R. E. M. Sample geometry and U uptake in archaeological teeth: implications for U-series and ESR dating. *Quaternary Sci Rev* **20**, 1021-1025 (2001). https://doi.org/10.1016/S0277-3791(00)00063-9

13 Balter, V. *et al.* U-Pb dating of fossil enamel from the Swartkrans Pleistocene hominid site, South Africa. *Earth Planet Sc Lett* **267**, 236-246 (2008). https://doi.org/10.1016/j.epsl.2007.11.039

14 Zhang, Y. Q. *et al.* The demise of the giant ape. *Nature* **625** (2024). https://doi.org/10.1038/s41586-023-06900-0

15 Sano, Y., Terada, K., Ly, C. V. & Park, E. J. Ion microprobe U-Pb dating of a dinosaur tooth. *Geochem J* **40**, 171-179 (2006). https://doi.org/10.2343/geochemj.40.171

16 Greene, S., Heaman, L. M., DuFrane, S. A., Williamson, T. & Currie, P. J. Introducing a geochemical screen to identify geologically meaningful U-Pb dates in fossil teeth. *Chem Geol* **493**, 1-15 (2018). https://doi.org/10.1016/j.chemgeo.2018.04.022

17 Woodhead, J. & Petrus, J. A. Exploring the advantages and limitations of in situ U-Pb carbonate geochronology using speleothems. *Geochronology* **1**, 69-84 (2019).

18 Halder, J., Terzer, S., Wassenaar, L. I., Araguás-Araguás, L. J. & Aggarwal, P. K. The Global Network of Isotopes in Rivers (GNIR): integration of water isotopes in watershed

observation and riverine research. *Hydrol Earth Syst Sc* **19**, 3419-3431 (2015). https://doi.org/10.5194/hess-19-3419-2015

19 Nagavciuc, V., Badaluta, C. A. & Ionita, M. Tracing the Relationship between Precipitation and River Water in the Northern Carpathians Base on the Evaluation of Water Isotope Data. *Geosciences* **9** (2019). https://doi.org/10.3390/geosciences9050198

20 Popescu, R. *et al.* Using stable isotopes in tracing contaminant sources in an industrial area: A case study on the hydrological basin of the Olt River, Romania. *Sci Total Environ* **533**, 17-23 (2015). https://doi.org/10.1016/j.scitotenv.2015.06.078

21 Horton, T. W., Defliese, W. F., Tripati, A. K. & Oze, C. Evaporation induced O and C enrichment in lake systems: A global perspective on hydrologic balance effects. *Quaternary Sci Rev* **131**, 365-379 (2016). https://doi.org/10.1016/j.quascirev.2015.06.030

22 Kohn, M. J. & Cerling, T. E. Stable isotope compositions of biological apatite. *Rev Mineral Geochem* **48**, 455-488 (2002). https://doi.org/10.2138/rmg.2002.48.12

23 van Dam, J. A. & Reichart, G. J. Oxygen and carbon isotope signatures in late Neogene horse teeth from Spain and application as temperature and seasonality proxies. *Palaeogeogr Palaeocl* **274**, 64-81 (2009). https://doi.org/10.1016/j.palaeo.2008.12.022

24 Hoppe, K. A., Stover, S. M., Pascoe, J. R. & Amundson, R. Tooth enamel biomineralization in extant horses: implications for isotopic microsampling. *Palaeogeogr Palaeocl* **206**, 355-365 (2004). https://doi.org/10.1016/j.palaeo.2004.01.012

25 Curran, S. *et al.* Multiproxy paleoenvironmental reconstruction of Early Pleistocene sites from the Olteț River Valley of Romania. *Palaeogeogr Palaeocl* **574**, 110445 (2021). https://doi.org/10.1016/j.palaeo.2021.110445

26 Huertas, A. D., Iacumin, P., Stenni, B., Chillon, B. S. & Longinelli, A. Oxygen-Isotope Variations of Phosphate in Mammalian Bone and Tooth Enamel. *Geochim Cosmochim Ac* **59**, 4299-4305 (1995).

27 Amiot, R. *et al.* Latitudinal temperature gradient during the Cretaceous Upper Campanian-Middle Maastrichtian: δO record of continental vertebrates. *Earth Planet Sc Lett* **226**, 255-272 (2004). https://doi.org/10.1016/j.epsl.2004.07.015

28 Bojar, A. V., Halas, S., Bojar, H. P. & Chmiel, S. Stable Isotope Hydrology of Precipitation and Groundwater of a Region with High Continentality, South Carpathians, Romania. *Carpath J Earth Env* **12**, 513-524 (2017).

29 Dragusin, V. *et al.* Transfer of environmental signals from the surface to the underground at Ascunsa Cave, Romania. *Hydrol Earth Syst Sc* **21**, 5357-5373 (2017). https://doi.org/10.5194/hess-21-5357-2017

30 IAEA/WMO. (2023).

31 Rozanski, K., Araguás-Araguás, L. & Gonfiantini, R. in *Geophysical Monograph Series* Vol. 78 (eds P. K. Swart, K. C. Lohmann, J. McKenzie, & S. Savin) 1-36 (1993).

32 Pryor, A. J. E., Stevens, R. E., O'Connell, T. C. & Lister, J. R. Quantification and propagation of errors when converting vertebrate biomineral oxygen isotope data to temperature for palaeoclimate reconstruction. *Palaeogeogr Palaeocl* **412**, 99-107 (2014). https://doi.org/10.1016/j.palaeo.2014.07.003

33 Domingo, L. *et al.* Late Neogene and Early Quaternary Paleoenvironmental and Paleoclimatic Conditions in Southwestern Europe: Isotopic Analyses on Mammalian Taxa. *Plos One* **8**, e63739 (2013). https://doi.org/10.1371/journal.pone.0063739

34 Cerling, T. E. & Harris, J. M. Carbon isotope fractionation between diet and bioapatite in ungulate mammals and implications for ecological and paleoecological studies. *Oecologia* **120**, 347-363 (1999). https://doi.org/10.1007/s004420050868
35 Kohn, M. J. Carbon isotope compositions of terrestrial C3 plants as indicators of (paleo)ecology and (paleo)climate. *P Natl Acad Sci USA* **107**, 19691-19695 (2010). https://doi.org/10.1073/pnas.1004933107
36 Kohn, M. J. & McKay, M. P. Paleoecology of late Pleistocene-Holocene faunas of eastern and central Wyoming, USA, with implications for LGM climate models. *Palaeogeogr Palaeocl* **326**, 42-53 (2012). https://doi.org/10.1016/j.palaeo.2012.01.037
37 Pollard, T. *et al.* DQPB : software for calculating disequilibrium U-Pb ages. *Geochronology* **5**, 181-196 (2023). https://doi.org/10.5194/gchron-5-181-2023
38 Malassé, A. D. *et al.* Intentional cut marks on bovid from the Quranwala zone, 2.6 Ma, Siwalik Frontal Range, northwestern India. *Cr Palevol* **15**, 317-339 (2016). https://doi.org/10.1016/j.crpv.2015.09.019
39 Sahnouni, M. *et al.* 1.9-million- and 2.4-million-year-old artifacts and stone tool-cutmarked bones from Ain Boucherit, Algeria. *Science* **362**, 1297-1301 (2018). https://doi.org/10.1126/science.aau0008
40 Sablin, M. V. & Iltsevich, K. Faunal complex of the Early Pleistocene Muhkai 2 locality. *Proceedings of the Zoological Institute RAS* **325**, 82-90 (2021).
41 Sablin, M. V. & Girya, E. Y. The earliest evidence of human occupation in Southeastern Europe: a processed camel bone fragment from the Lower Don. *Archaeology, Ethnology and Anthropology of Eurasia* **38**, 7-13 (2010).
42 Tappen, M., Bukhsianidze, M., Ferring, R., Coil, R. & Lordkipanidze, D. Life and death at Dmanisi, Georgia: Taphonomic signals from the fossil mammals. *J Hum Evol* **171**, 103249 (2022). https://doi.org/10.1016/j.jhevol.2022.103249
43 Vislobokova, I. A., Agadzhanyan, A. K. & Lopatin, A. V. The case of Trlica TRL11-10 (Montenegro): Implications for possible early hominin dispersals into the Balkans in the middle of the Early Pleistocene. *Quatern Int* **554**, 15-35 (2020). https://doi.org/10.1016/j.quaint.2020.06.025
44 Sahnouni, M. *et al.* The first evidence of cut marks and usewear traces from the Plio-Pleistocene locality of El-Kherba (Ain Hanech), Algeria: implications for early hominin subsistence activities circa 1.8 Ma. *J Hum Evol* **64**, 137-150 (2013). https://doi.org/10.1016/j.jhevol.2012.10.007
45 Cheheb, R. C. *et al.* Human behavior and Homo-mammal interactions at the first European peopling: new evidence from the Pirro Nord site (Apricena, Southern Italy). *Sci Nat-Heidelberg* **106**, 16 (2019). https://doi.org/10.1007/s00114-019-1610-4
46 Yeshurun, R., Zaidner, Y., Eisenmann, V., Martinez-Navarro, B. & Bar-Oz, G. Lower Paleolithic hominin ecology at the fringe of the desert: Faunal remains from Bizat Ruhama and Nahal Hesi, Northern Negev, Israel. *J Hum Evol* **60**, 492-507 (2011). https://doi.org/10.1016/j.jhevol.2010.01.008
47 Gaudzinski, S. Subsistence patterns of Early Pleistocene hominids in the Levant-taphonomic evidence from the 'Ubeidiya Formation (Israel). *J Archaeol Sci* **31**, 65-75 (2004). https://doi.org/10.1016/S0305-4403(03)00100-6
48 Choi, K. & Driwantoro, D. Shell tool use by early members of *Homo erectus* in Sangiran, central Java, Indonesia: cut mark evidence. *J Archaeol Sci* **34**, 48-58 (2007). https://doi.org/10.1016/j.jas.2006.03.013

49 Espigares, M. P. *et al.* The earliest cut marks of Europe: a discussion on hominin subsistence patterns in the Orce sites (Baza basin, SE Spain). *Sci Rep-Uk* **9**, 15408 (2019). https://doi.org/10.1038/s41598-019-51957-5

50 Gallotti, R. *et al.* First high resolution chronostratigraphy for the early North African Acheulean at Casablanca (Morocco). *Sci Rep-Uk* **11**, 15340 (2021). https://doi.org/10.1038/s41598-021-94695-3

51 Echassoux, A. Taphonomy, palaeoecology and zooarchaeology of the lower Pleistocene mammals of Vallonnet cave (Roquebrune-Cap-Martin, Alpes-Maritimes, France). *Anthropologie* **108**, 11-53 (2004). https://doi.org/10.1016/j.anthro.2004.01.006

52 Michel, V. *et al.* New dating evidence of the early presence of hominins in Southern Europe. *Sci Rep-Uk* **7**, 10074 (2017). https://doi.org/10.1038/s41598-017-10178-4

53 Huguet, R. *et al.* Level TE9c of Sima del Elefante (Sierra de Atapuerca, Spain): A comprehensive approach. *Quatern Int* **433**, 278-295 (2017). https://doi.org/10.1016/j.quaint.2015.11.030